

Catalyst-Agent: Autonomous heterogeneous catalyst screening and optimization with an LLM Agent

Achuth Chandrasekhar,[†] Janghoon Ock,[‡] and Amir Barati Farimani^{*,†,¶,§,||,⊥}

[†]*Mechanical Engineering, Carnegie Mellon University, Pittsburgh, PA 15213, USA*

[‡]*Department of Chemical and Biomolecular Engineering, University of Nebraska–Lincoln, Lincoln, NE 68588, USA*

[¶]*Biomedical Engineering, Carnegie Mellon University, Pittsburgh, PA 15213, USA*

[§]*Chemical Engineering, Carnegie Mellon University, Pittsburgh, PA 15213, USA*

^{||}*Materials Science and Engineering, Carnegie Mellon University, Pittsburgh, PA 15213, USA*

[⊥]*Machine Learning Department, Carnegie Mellon University, Pittsburgh, PA 15213, USA*

E-mail: barati@cmu.edu

Abstract

The discovery of novel catalysts tailored for particular applications is a major challenge for the twenty-first century. Traditional methods for this include time-consuming and expensive experimental trial-and-error approaches in labs based on chemical theory or heavily computational first-principles approaches based on density functional theory. Recent studies show that deep learning models like graph neural networks (GNNs) can significantly speed up the screening and discovery of catalyst materials by many orders of magnitude, with very high accuracy and fidelity. In this work, we introduce Catalyst-Agent, a Model Context Protocol (MCP) server-based, LLM-powered

AI agent. It can explore vast material databases using the OPTIMADE API, make structural modifications, calculate adsorption energies using Meta FAIRchem’s UMA (GNN) model, via FAIRchem’s AdsorbML workflow and slab construction, and make useful material suggestions to the researcher in a closed-loop manner, including surface-level modifications to refine near-miss candidates. It is tested on three pivotal reactions: the oxygen reduction reaction (ORR), the nitrogen reduction reaction (NRR), and the CO₂ reduction reaction (CO₂RR). Catalyst-Agent achieves a success rate of 23–34% among all the materials it chooses and evaluates, and manages to converge in 1–2 trials per successful material on average. This work demonstrates the potential of AI agents to exercise their planning capabilities and tool use to operationalize the catalyst screening workflow, provide useful, testable hypotheses, and accelerate future scientific discoveries for humanity with minimal human intervention.

1 Introduction

Designing optimal catalyst materials is a central challenge in chemical technology.^{1–3} Catalyst discovery has traditionally proceeded through iterative experimental cycles of hypothesis, synthesis and performance measurement, with substantial time and monetary expenditure. Experimental researchers synthesize novel materials and characterize their activity, selectivity and stability, while computational researchers use first-principles electronic-structure calculations to predict catalytic trends before synthesis. Density functional theory (DFT) enables estimation of adsorption energies, activation barriers and other energetic descriptors on well-defined catalytic surfaces, supporting scaling relations and mechanistic insights.^{4,5} Despite this progress, conventional catalyst screening remains bottlenecked by the creation of physically consistent surface models and the execution of expensive calculations across diverse materials, facets and adsorption sites.

The adsorption energy quantifies the thermodynamic driving force for adsorbate binding to a catalytic surface and corresponds to the global minimum energy over all configura-

tions:⁶⁻⁸

$$\Delta E_i = E_{\text{slab}+i} - E_{\text{slab}} - E_{\text{gas}}, \quad (1)$$

$$\Delta E_{\text{ads}} = \min(\Delta E_i) \quad (2)$$

where $E_{\text{slab}+i}$ is the total energy of the relaxed adsorbate–slab system, E_{slab} is the energy of the clean slab, and E_{gas} is the gas-phase adsorbate reference energy. Negative ΔE_{ads} values indicate stronger binding, while positive values indicate weaker adsorption. Because adsorption energies of key intermediates correlate with rate-determining steps, they are widely adopted as activity and selectivity descriptors.

Finding the global minimum energy across all configurations demands orchestrating multiple calculations over surface terminations, spin states and numerical settings.⁹⁻¹¹ High-throughput computational catalysis has focused on automating these evaluations across material families, but even with automation DFT relaxations remain slow (approximately 48 hours each), and the combinatorics of facets, sites and adsorbates multiplies this cost. This has motivated machine learning (ML) surrogate models that approximate DFT at a fraction of the computational expense.¹²⁻¹⁸ Among the various ML approaches, atomistic models that operate directly on atomic geometries are especially attractive. Graph Neural Networks (GNNs), which represent atoms as nodes and bonds as edges to capture local chemical environments, are particularly effective for predicting energies and forces of atomic systems.¹⁹⁻²⁵ Building on progress in GNNs, Universal machine-learned interatomic potentials (U-MLIPs) have been made possible by large databases consisting of DFT calculations and ab-initio molecular dynamics simulations (AIMD).²⁶⁻²⁸

The AdsorbML framework by Lan et al. formalizes ML-accelerated adsorption evaluation by providing tools for slab construction, adsorbate placement, relaxation and energy computation. ML potentials relax catalyst-adsorbate systems from initial configurations. The

FAIRchem initiative from Meta²⁹ extends this ecosystem with the UMA family of universal ML interatomic potentials,²⁵ which provide transferable energy and force predictions across diverse chemistries. In this work, we employ the UMA small model (uma-s-1p1) as the primary surrogate within the AdsorbML workflow. First-principles validation is not eliminated but moved downstream to confirm ML-shortlisted candidates with higher-fidelity DFT calculations and experiments.

Modern deep learning has also developed the transformer architecture, introduced in the seminal “Attention Is All you Need” work, which has revolutionized natural language processing.³⁰ This architecture forms the backbone of large language models (LLMs) capable of advanced reasoning over goals, constraints and intermediate results in natural language. This creates an opportunity to connect scientific workflows with deep learning architectures that can predict outcomes in an iterative fashion.^{31–37} For catalyst discovery, this opens the possibility of an autonomous agent that retrieves structures, evaluates energetics and refines candidates in response to quantitative feedback.

Recent studies have endeavored to explore this intersection. CatGPT by Mok and Back,³⁸ a fine-tuned GPT-2³⁹ autoregressive model, generates heterogeneous catalyst surface structures as text sequences encoding lattice parameters, elemental symbols and fractional coordinates. Controllable generation is achieved through adsorbate-conditioned prompts, with validity filtering via a BERT-based⁴⁰ anomaly detector and validation using EquiformerV2²⁰ and finally DFT, though the approach focuses on structure proposal rather than closed-loop energetic optimization. ChemReasoner by Sprueill et al.⁴¹ reframes screening as LLM-guided search with quantum-chemical feedback via beam search and context-aware planning;⁴² the physics-informed reward steers exploration and reduces hallucination risk, though the system relies on simplifying assumptions for 3D structure conversion and a less accurate reward model than current universal potentials. Yao et al.⁴³ presented an “LLM to Agent” framework for MgH₂ catalyst design combining literature mining⁴⁴ with supervised ML prediction and SHAP-based interpretability.⁴⁵ These efforts establish that LLMs can contribute to cat-

alyst discovery, but none provides a fully autonomous, tool-grounded framework spanning database retrieval through iterative surface refinement within a single closed-loop pipeline.

The Model Context Protocol (MCP) framework⁴⁶ addresses this gap by providing a standardized interface for exposing external servers with tools and resources to an AI agent with tool-augmented reasoning. Agentic AI is poised to revolutionize scientific discovery.^{47–56} For catalyst discovery, MCP modularizes the end-to-end workflow: database queries, geometry construction, ML relaxation and energy evaluation into structured tools with defined inputs and outputs, improving transparency and reproducibility. Critically, this modular server architecture also resolves the practical challenge of conflicting software dependencies that arise when integrating heterogeneous computational tools (database clients, ML frameworks, atomistic simulation libraries) within a single pipeline. In addition, the generous free tiers and rate limits offered by current LLM API providers render short-to-moderate screening campaigns feasible at negligible marginal cost, substantially lowering the barrier to entry for researchers pursuing exploratory computational catalysis, though longer or larger-scale campaigns will incur proportionally higher API expenses. This enables closed-loop operation where the agent adaptively refines its search strategy based on tool outputs rather than relying on free-form generation alone.

In this study, we introduce Catalyst-Agent, an autonomous AI agent that addresses this gap by integrating tool-augmented LLM planning with ML-accelerated adsorption energy evaluation to enable end-to-end catalyst screening and optimization. Unlike prior approaches that focus on structure generation³⁸ or literature mining,⁴³ Catalyst-Agent retrieves candidate crystals from established databases, constructs physically consistent surface models, evaluates adsorption energetics through the UMA-powered AdsorbML pipeline and iteratively refines near-miss candidates via surface modifications. All of this is orchestrated autonomously within a single closed-loop MCP-based framework. We evaluate Catalyst-Agent on three electrocatalytic screening tasks: the oxygen reduction reaction (ORR), nitrogen reduction reaction (NRR) and CO₂ reduction reaction, and demonstrate its effectiveness

across chemically diverse search spaces.

2 Results and discussion

2.1 Catalyst-Agent operation: MCP servers with an LLM Agent for iterative catalyst screening and optimization

Catalyst-Agent’s main contribution is an operational framework, shown in Figure 1, that operates in a closed-loop in which high-level screening goals serve as rewards to drive tool-grounded adsorption energy calculations. Rather than consolidating all capabilities into a single monolithic tool server, the framework distributes its functionality across five specialized Model Context Protocol (MCP)⁴⁶ servers, each encapsulating a distinct stage of the catalyst screening pipeline. This is done to efficiently manage diverse and often clashing dependencies and packages. An LLM-based agent, powered by GPT-5.2 running inside the Codex CLI environment,⁵⁷ acts as the central orchestrator: it receives a user prompt specifying a target reaction, adsorbates and activity criteria, and then plans, sequences and invokes the appropriate MCP server tools to execute the end-to-end screening workflow.

Each MCP server exposes a well-defined set of tools as shown in Table 1, with predefined input schemas and structured JSON outputs, enabling the agent to invoke them through a request/response command-line interface and to feed the returned results directly into subsequent reasoning steps within its model context. A key architectural principle is isolation: the tool endpoints act as lightweight proxies that outsource computationally intensive tasks (database queries, GPU-accelerated relaxations) to external processes, thereby preventing GPU overloading, enabling fine-grained error handling and ensuring that a failure in one server does not crash the entire system. Frequent JSON-based logging keeps the supervisor LLM informed of execution status at every stage.

The end-to-end closed-loop flowchart is depicted in Figure 1b. Beginning with a user prompt that specifies the target reaction and adsorbates, the agent proceeds through the

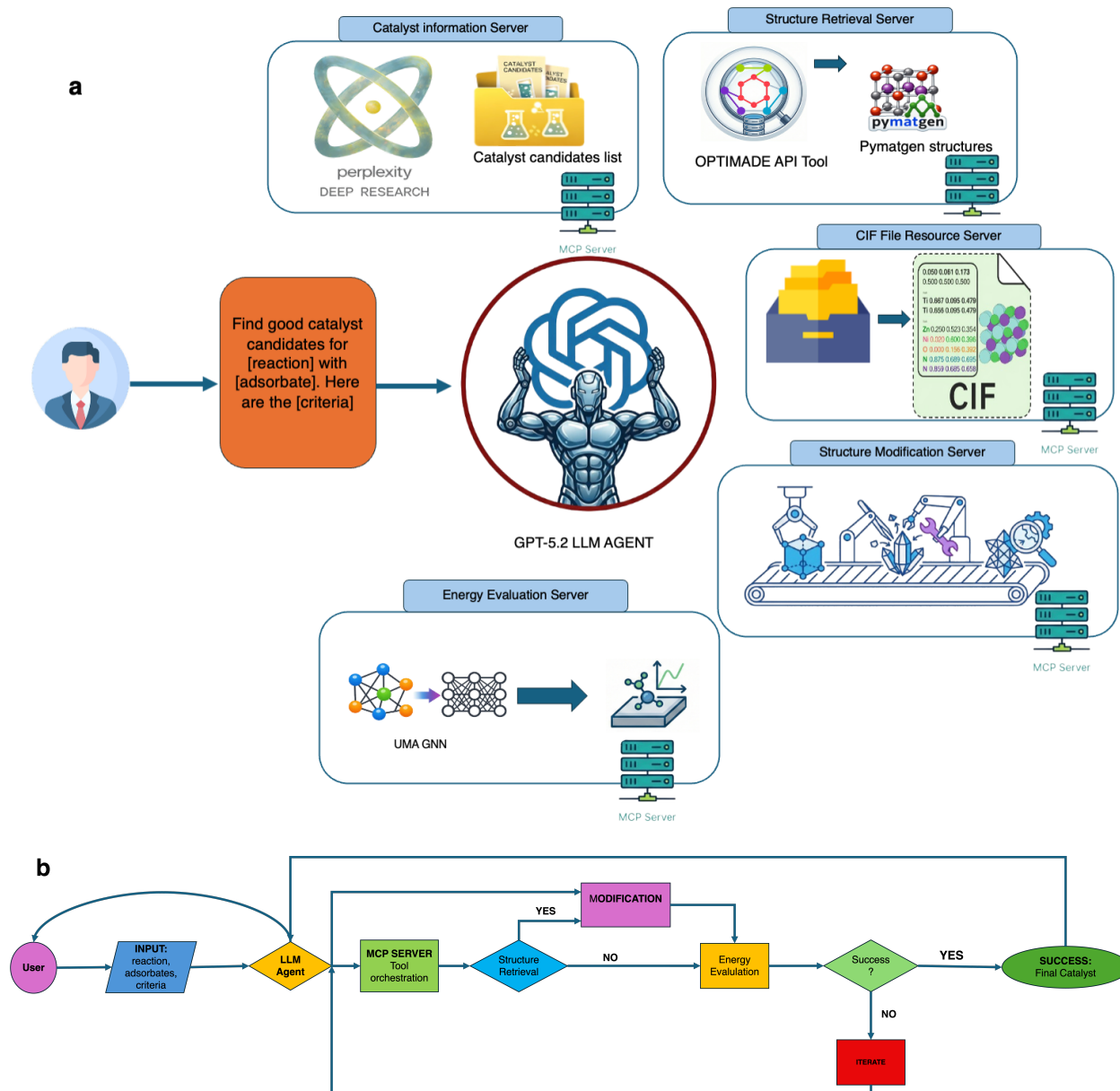


Figure 1: Overview of Catalyst-Agent: (a) the LLM Agent supervisor acts as the chief orchestrator and the five specialized MCP servers act as the operating limbs (b) the end-to-end flowchart showing structure retrieval, modification, evaluation, and iteration.

following stages: obtaining an initial candidate list, retrieving crystal structures, optionally applying surface modifications, evaluating adsorption energies via the AdsorbML-UMA pipeline, checking whether the computed descriptors satisfy the acceptance criteria, and, if the result is a near-miss, iterating back to modify the surface and re-evaluate. The following subsections describe each of the five MCP servers in detail. A complete example of the

MCP tool-call sequence and JSON outputs for a single material screening is provided in Section S2, and a representative user prompt is given in Section S1.

Table 1: MCP servers and their exposed tools in the Catalyst-Agent framework.

Server	Tools
Catalyst Information (Perplexity Deep Research)	<code>deep_research</code>
Structure Retrieval	<code>optimade_structure_search</code>
CIF File Resource	<code>list_cif_files</code>
Structure Modification	<code>create_and_serialize_slab</code>
Energy Evaluation	<code>adsorbml_evaluate</code>

2.1.1 Catalyst Information Server

The Catalyst Information Server provides the agent with an initial seeded list of candidate materials for a given reaction. For the ORR and NRR screening campaigns, the candidate lists are generated using Perplexity’s Deep Research,⁵⁸ which aggregates literature-informed suggestions of promising elemental compositions. These lists are supplied to the agent as file links through the user prompt. Considering the rarity of stable surfaces and viable materials for the CO₂ reduction reaction, the initial candidate list for CO₂RR is instead obtained from the Stanford SUNCAT surface reaction database, known as Catalysis Hub.⁵⁹ Manual filtering is employed, as many reaction-specific material entries are missing in this database. This server thus acts as the entry point of the screening pipeline, furnishing the agent with a curated starting pool of chemistries to explore. A user guidance prompt is also passed to the agent at this stage to specify the operational requirements, target adsorbates and descriptor criteria for success.

2.1.2 Structure Retrieval Server

The Structure Retrieval Server exposes tools that query the OPTIMADE API⁶⁰ to retrieve inorganic crystalline structures from multiple databases. In this work, two providers are used: the Materials Project⁶¹ and the Open Quantum Materials Database (OQMD).^{62,63}

The agent supplies element names and the number of distinct elements in the target formula, and the server returns matching structures. Other OPTIMADE-accessible databases such as the Alexandria Materials Database and the Crystallography Open Database⁶⁴ are also compatible but were not queried in this study to limit computational overhead.

The server returns two complementary outputs: (i) a master record containing complete, serializable pymatgen⁶⁵ structure representations (formula, space group, lattice parameters, atomic positions and other structural metadata), and (ii) a compact summary intended for perusal by the LLM supervisor, which reduces the textual volume to simplify material selection and prevent overflow of the LLM’s context window. The master record structures can be converted to ASE Atoms objects⁶⁶ for direct use in FAIRchem’s AdsorbML workflow.¹⁰

2.1.3 CIF File Resource Server

The CIF File Resource Server provides an alternative pathway for supplying crystal structures to the pipeline. Instead of querying online databases, the agent or the user can supply a direct link to a Crystallographic Information File (CIF).⁶⁷ When a CIF file is used, the server automatically performs symmetry analysis on the input structure with *symprec* = 1.5, and logs the crystallographic space group symbol and number. This metadata is included in the returned results JSON alongside the parsed structure, ensuring full provenance tracking. The CIF pathway is particularly useful for materials that may not yet be indexed in OPTIMADE providers or for user-defined custom structures.

2.1.4 Structure Modification Server

The Structure Modification Server enables the agent to apply targeted surface-level modifications to a candidate slab before adsorption energy evaluation, as illustrated in Figure 2. This server supports two modification modes:

1. **Top-layer substitution (doping):** A single atom in the topmost surface layer is identified by its fractional z coordinate and replaced with a new element. This is

inspired by the approach of Sun et al.⁶⁸ This modifies the local electronic structure of the active site and alters the adsorption environment without changing the bulk crystal identity.

2. **In-plane strain:** The a and b lattice vectors of the slab are uniformly scaled by $(1 - \varepsilon)$, where $\varepsilon > 0$ corresponds to compressive strain and $\varepsilon < 0$ to tensile strain, in a manner similar to Oliveira et al.⁶⁹ The c lattice vector (vacuum direction) is left unchanged to preserve the slab geometry.

These modifications are lightweight, rapid to apply and enable the agent to iteratively refine near-miss candidates. The agent autonomously decides which modification to attempt and with what parameters (substitution element, strain magnitude) based on the energetic feedback from previous iterations. All applied modifications are recorded in the results JSON for full traceability.

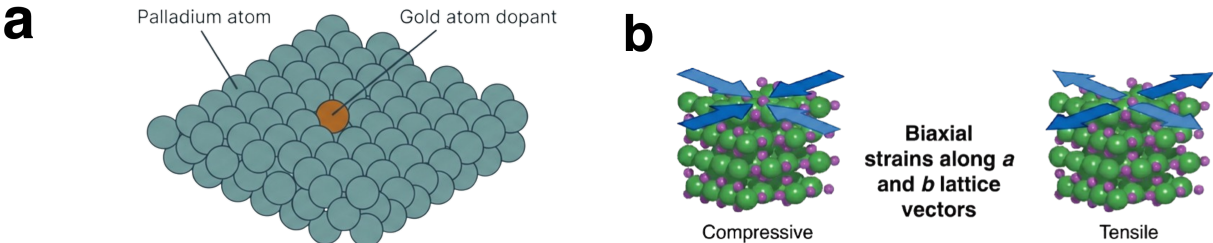


Figure 2: Optional surface-level modifications for catalysis after slab construction: (a) Top-layer substitution (doping) and (b) in-plane strain applied to the surface slab. All applied modifications are recorded in the results JSON.

2.1.5 Energy Evaluation Server

The Energy Evaluation Server is the computational core of Catalyst-Agent. It accepts a candidate structure (either from the Structure Retrieval Server’s cache, a CIF input or an ASE Atoms object from the modification server) together with an adsorbate label and up to five Miller indices per tool call, and evaluates adsorption energies on all requested facets *in parallel*. This multi-facet design substantially improves the agent’s throughput and provides a simultaneous “multi-facet snapshot” of a material’s surface chemistry.

Internally, for each requested Miller index, the server constructs an oriented slab that satisfies minimum lateral size requirements and tags atoms for downstream adsorbate placement and relaxation. The minimum in-plane tiling threshold (`min_ab`) is chosen adaptively: 8.0 Å for low-index facets ($\max(|h|, |k|, |l|) \leq 3$) and 6.0 Å otherwise, improving robustness for high-index surfaces. Detailed debug information is returned if slab tiling fails, enabling expedited handling of unrealistic geometries.

Adsorption energies are computed through the AdsorbML workflow using the UMA small (`uma-s-1p1`) MLIP to relax multiple initial adsorbate placements per slab. The relaxations use a quasi-Newton optimizer (LBFGS) under predetermined convergence criteria (force tolerance `fmax=0.05 eV/Å` and `number of steps=300`). Each evaluation returns a structured JSON summary containing: (i) the total number of attempted configurations, (ii) the number of valid configurations, (iii) the number of detected anomalies, and (iv) the global minimum adsorption energy prediction among the valid runs, including energy splits that decompose the total into slab, gas-phase reference and adsorbate–slab system contributions. Five adsorbate placements are used for an initial round of high-level screening across all materials. Successful candidates from this round are subjected to a second round of thirty placements for refined evaluation and the finalization of the recommended catalysts.

The parallel execution structure is coupled with meticulous post-processing to preserve information fidelity. Results for each material are returned as a single JSON object containing the adsorbate label, the requested structure reference details and a master dictionary

of per-facet outcomes including energy minima and flagged anomalies. Subprocess isolation ensures that individual facet failures are contained and reported without disrupting the remaining evaluations.

2.1.6 Closed-loop iteration summary

The high-level overview of the closed-loop process orchestrated by the agent across these five servers is: propose candidate chemistries (Catalyst Information Server) → retrieve crystal structures (Structure Retrieval Server or CIF File Resource Server) → evaluate adsorption energies on multiple facets (Energy Evaluation Server) → compare to descriptor criteria → if the candidate is a near-miss but promising, apply strain or substitution doping (Structure Modification Server) → re-evaluate (Energy Evaluation Server), iterating until the activity criteria are met or the candidate base material is deemed unsuitable for further modification. The agent is prompted to document its reasoning behind material selection and any modifications applied.

2.2 Target reactions, adsorbates, and descriptor definitions

Catalyst-Agent was evaluated on three representative screening tasks. Each of these reactions is defined by a set of adsorbates and quantitative activity descriptors. All these quantities are obtained from the UMA-powered AdsorbML pipeline, summarized by the minimum-energy valid configuration for a given material-adsorbate system. Table 2 summarizes the targeted reactions, the adsorbates evaluated, and the descriptors used for decision making.

Table 2: Targeted reactions, AdsorbML adsorbates, and descriptor criteria used by Catalyst-Agent in each screening campaign. Energies are in eV.

Task	Adsorbates	Descriptor(s)	Acceptance / Target Criterion
Oxygen Reduction Reaction (ORR)	*OH	$E_{\text{ads}}(*\text{OH})$	Target window: 0.9–1.1 eV
CO ₂ Reduction to CO (CO ₂ RR)	*CO, *H	$E_{\text{ads}}(*\text{CO}), E_{\text{ads}}(*\text{H})$	$E_{\text{ads}}(*\text{CO}) \in [-0.82, -0.52]$ and $E_{\text{ads}}(*\text{H}) \geq 0.33$
Nitrogen Reduction (NRR)	*N, *N ₂	$E_{\text{ads}}(*\text{N}), E_{\text{ads}}(*\text{N}_2), \Delta$	$E_{\text{ads}}(*\text{N}) \in [-2.0, -0.5]$ and $\Delta = E_{\text{ads}}(*\text{N}) - E_{\text{ads}}(*\text{N}_2) > 0$

The choices of descriptors here reflect common mechanistic heuristics but are simple enough to support autonomous and high-throughput iterations. For oxygen electrocatalysis, *OH adsorption energy readily provides an approximate indicator of binding strength, and the optimal band of (0.9-1.1 eV) is chosen for proximity to the adsorption energy of *OH on the Pt (111) surface.⁷⁰ Scaling relationships are given in great detail by Man et al.⁷¹ and similarity of mechanism to Pt is noted by Wang et al.⁷² For CO₂RR, the multiple conditions for the adsorption energies of *CO and *H give a dual constraint: *CO must bind strongly enough to form but not so strongly as to poison the catalytic surface, while $E_{\text{ads}}*\text{H}$ must be sufficiently unfavorable to suppress the competitive hydrogen evolution reaction (HER) under the same conditions. These descriptors are the same as those utilized by Song et al.⁷³ For the Nitrogen Reduction Reaction (NRR), the atomic-molecular descriptor Δ identifies surfaces that stabilize the atomic nitrogen intermediate (*N) relative to adsorbed N₂, and simultaneously, a moderate $E_{\text{ads}}*\text{N}$ window is applied to avoid non-binding and irreversible trapping.⁷⁴ Naturally, Catalyst-Agent is able to perform iterative strain and doping substitution tests for promising candidates that fall near, but not quite inside the acceptable boundaries. The complete raw screening outputs for all three reactions are listed in Section S3, and the human-curated classification of successful and failed candidates is

presented in Section S4.

2.3 Closed-loop screening effectiveness across tasks

To quantify Catalyst-Agent’s screening effectiveness, we report several complementary metrics computed across the three reaction campaigns. These metrics capture distinct aspects of performance: (i) the success rate, the fraction of tested materials satisfying the target descriptors; (ii) the trials-to-success distribution, the number of evaluation attempts required before reaching success (iii) the modification frequency, the fraction of materials in each outcome category (successful or failed) that required at least one surface modification; and (iv) per-material counts of successful and unsuccessful modifications among materials that entered the modification loop (Total Trials > 1). A “trial” corresponds to a single adsorption-energy evaluation for a specific material–adsorbate configuration (material, surface facet, and optional strain or top-layer substitution).

Let N_{tot} be the total number of distinct materials evaluated for a given reaction screening task and let N_{succ} be the number of materials for which at least one attempted condition satisfies the target descriptors. The success rate is:

$$R_{\text{succ}} = \frac{N_{\text{succ}}}{N_{\text{tot}}}. \quad (3)$$

For each successful material i , let t_i denote the number of trials required until the first successful condition is found (counting from the base, unmodified condition and including any subsequent facets and modification attempts). The average trials-to-success is then:

$$\bar{t}_{\text{succ}} = \frac{1}{N_{\text{succ}}} \sum_{i=1}^{N_{\text{succ}}} t_i. \quad (4)$$

The modification frequency for a given outcome category (successful or failed materials)

is the fraction of materials whose total trial count exceeds one:

$$f_{\text{mod}} = \frac{N_{\text{mod}}}{N_{\text{cat}}}, \tag{5}$$

where N_{mod} is the number of materials with Total Trials > 1 in the category and N_{cat} is the total number of materials in that category. For materials that enter the modification loop, we further report the mean number of successful modifications and unsuccessful modifications per material, along with their standard deviations.

Together, R_{succ} captures coverage, \bar{t}_{succ} captures efficiency, while f_{mod} and the per-material modification counts characterize the agent’s iterative refinement behaviour and its differential productivity across outcome categories.

Table 3: Closed-loop screening outcomes across tasks. R_{succ} is the fraction of tested materials that achieved at least one condition satisfying the task’s descriptor criteria. \bar{t}_{succ} is the mean number of trials required to reach the first success, averaged over successful materials; σ_t is the corresponding standard deviation quantifying inter-material variability. N_{tot} is the total number of distinct materials evaluated per task. The full distribution of trials-to-success is shown in the plot in Figure 3(b).

Task	N_{tot}	R_{succ}	\bar{t}_{succ}	σ_t
ORR (via *OH descriptor)	82	0.34	1.86	1.46
NRR (via *N/*N ₂ descriptors)	52	0.23	2.08	1.38
CO ₂ RR (via *CO/*H descriptors)	13	0.31	1.25	0.50

Table 4: Mean number of successful and unsuccessful surface modifications per material among only those materials that entered the modification loop (Total Trials > 1), stratified by material outcome (success vs. failure) and reaction task. Values are reported as mean±standard deviation. n is the number of modified materials in each category; the total number of materials in each outcome category is given in parentheses for reference. Full distributions are shown as plots in Figure 4.

Task	Modified successful materials			Modified failed materials		
	n	Succ. mods	Unsucc. mods	n	Succ. mods	Unsucc. mods
ORR	9 (28)	1.67±0.71	1.00±0.87	8 (54)	0.50±0.76	1.00±0.53
NRR	6 (12)	1.17±0.41	1.00±1.10	9 (40)	1.22±0.83	1.78±1.72
CO ₂ RR	1 (4)	1.00±0.00	0.00±0.00	9 (9)	2.00±1.50	2.33±1.58

Multiple trends are evident from Table 3 (per-material data are given in Sections S3 and S4). The success rates span a comparable range across the three case-study reactions ($R_{\text{succ}} \sim 0.23\text{--}0.34$), confirming that the agent’s operational loop can consistently locate promising candidates meeting the user-defined descriptors across chemically distinct search spaces. CO₂RR exhibits the lowest \bar{t}_{succ} (1.25 ± 0.50), indicating that successful candidates for CO₂RR are identified rapidly with minimal iteration and tight inter-material consistency. In contrast, ORR and NRR show higher mean trials (1.86 ± 1.46 and 2.08 ± 1.38 , respectively), reflecting a greater need for multi-facet exploration and iterative surface modifications to land within their respective narrow target regions. The plot in Figure 3(b) shows that the trials-to-success distribution is right-skewed for ORR and NRR: many materials succeed on the first baseline evaluation, while a subset requires several rounds of strain or doping modifications. NRR displays the lowest success rate (0.23) among the three tasks, consistent with the stricter, multi-descriptor acceptance criterion that simultaneously requires moderate *N binding and a favourable $\Delta = E_{\text{ads}}(*\text{N}) - E_{\text{ads}}(*\text{N}_2) > 0$.

An overview of the screening campaign statistics is presented in Figure 3. Panel (a) visualizes the success rate for each reaction, panel (b) shows the distribution of trials-to-success for successful materials as a plot (reflecting substantial inter-material variability),

and panel (c) compares the fraction of materials that required at least one surface modification between successful and failed material categories. For ORR, 32% of successful materials required modifications compared to only 15% of failures, indicating that the agent’s iterative refinement loop is a meaningful contributor to expanding the pool of viable candidates beyond what the unmodified base structures alone would provide. For NRR, this contrast is even more pronounced: 50% of successful materials needed modification versus 23% of failures, underscoring the challenging multi-descriptor landscape and the value of adaptive surface engineering. For CO₂RR, all failure materials (100%) underwent multiple modification attempts, while only 25% of successful materials required any modification; this asymmetry reflects the agent’s persistent but ultimately unproductive effort to rescue intrinsically unsuitable candidates through surface tuning.

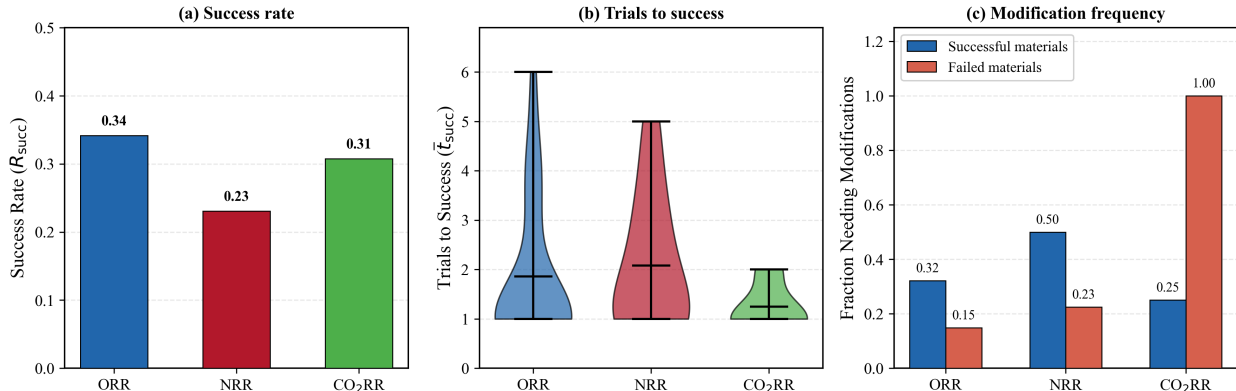


Figure 3: Screening campaign overview across the three target reactions. (a) Success rate R_{succ} . (b) Distribution of trials to first success for successful materials, horizontal lines indicate mean and min–max range. (c) Fraction of materials that required at least one surface modification (trial count > 1), compared between successful and failed material categories.

Surface modification effort: Beyond the coarse trial counts, we characterize the agent’s modification behaviour in greater detail. Because the majority of materials are resolved on the first baseline evaluation without any modification, reporting modification statistics over the full population dilutes the signal from the iterative refinement loop. We therefore restrict the modification analysis to only those materials that entered the modification loop (i.e.

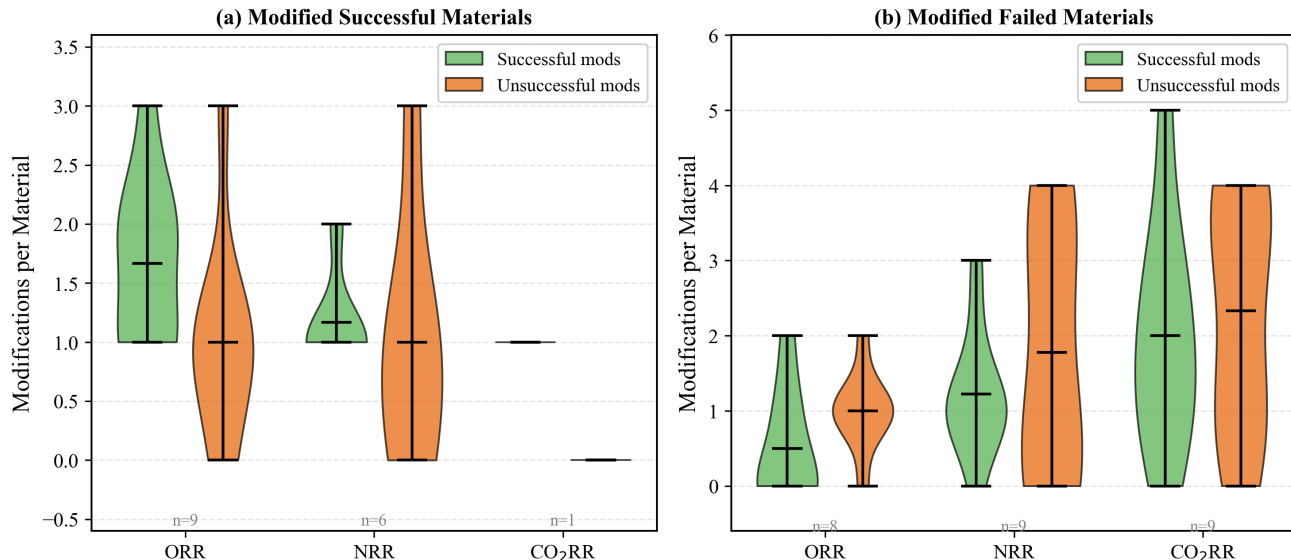


Figure 4: Distribution of successful and unsuccessful surface modifications per material among materials that entered the modification loop (Total Trials > 1), grouped by outcome category: (a) modified successful materials and (b) modified failed materials. Plots show the full distribution with mean and min–max range; sample sizes n are annotated below each group. The contrast between panels highlights the differential modification productivity across outcome categories.

Total Trials > 1), which isolates the subset of candidates for which the agent actively applied surface engineering. A “successful modification” is defined as one where the modified surface produced at least one facet satisfying the descriptor criteria. An “unsuccessful modification” is one where no facet met the acceptance threshold after applying the modification. Table 4 reports the mean and standard deviation of successful and unsuccessful modifications per material, conditioned on entry into the modification loop.

Several informative patterns emerge from Table 4 and the corresponding plots in Figure 4. First, among ORR materials that entered the modification loop, successful materials averaged 1.67 ± 0.71 successful modifications compared to only 0.50 ± 0.76 for failure materials. This roughly 3:1 contrast demonstrates that surface modifications: doping and strain, are effective tuning strategies when the base material already possesses a favourable electronic structure that places it near the descriptor boundary. Materials that are intrinsically far from the target window cannot be rescued by a comparable number of surface-level per-

turbations and instead accumulate more unsuccessful attempts (1.00 ± 0.53 for failures vs. 1.00 ± 0.87 for successes in ORR, with the failures showing tighter clustering around a single failed attempt).

Second, for NRR the distinction between success and failure modification outcomes is less pronounced: modified successful materials averaged 1.17 ± 0.41 successful modifications, while modified failure materials averaged 1.22 ± 0.83 . However, the key differentiator is in the unsuccessful modifications, where failures accumulated 1.78 ± 1.72 unsuccessful attempts compared to 1.00 ± 1.10 for successes. This asymmetry reflects the more restrictive multi-descriptor acceptance criterion for NRR: the agent explores aggressively, but the narrow joint acceptance window (*N binding condition plus the $\Delta > 0$ constraint) means that even chemically reasonable modifications frequently fail to satisfy all criteria simultaneously.

Third, for CO₂RR the modification landscape is qualitatively different. All nine failure materials entered the modification loop (reflecting the challenging nature of the Catalysis Hub-derived candidate pool), accumulating 2.00 ± 1.50 successful and 2.33 ± 1.58 unsuccessful modifications per material. The agent invested significant effort into these candidates, including up to 10 trials for Al₃Ni, before moving on, reflecting a persistent but ultimately non-convergent optimization trajectory for intrinsically mismatched candidates. In contrast, only one of four CO₂RR successful materials required any modification, and that single case (LaTl₃) was resolved with one successful modification and zero unsuccessful ones.

Fourth, the ratio of successful to unsuccessful modifications among modified materials provides a direct measure of the agent’s “hit rate” in selecting productive modifications. For ORR modified successful materials, this ratio is 1.67:1.00, indicating that the agent selects productive modifications more often than not. For NRR modified successful materials, the ratio is 1.17:1.00, still favourable but reflecting a more exploratory search consistent with the tighter multi-descriptor acceptance criterion.

Trial distribution analysis: To provide deeper insight into the per-material convergence behaviour, Figure 5 presents plots of the number of trials per material, separated by reaction and outcome category. For ORR and NRR successful materials, the mean trial count is low (1.86 and 2.08, respectively), but the distributions exhibit right-skewed tails extending to 5–6 trials, confirming that a minority of near-miss materials require substantial iterative refinement. In contrast, the CO₂RR failure distribution is markedly right-shifted (mean ≈ 4 , range 3–10), reflecting the agent’s persistent but unsuccessful attempts to modify intrinsically unsuitable candidates. These distributional characteristics complement the summary statistics in Table 3 and provide evidence that the iterative modification loop is not uniformly applied but is instead adaptively allocated by the agent in proportion to the perceived proximity of each candidate to the descriptor target.

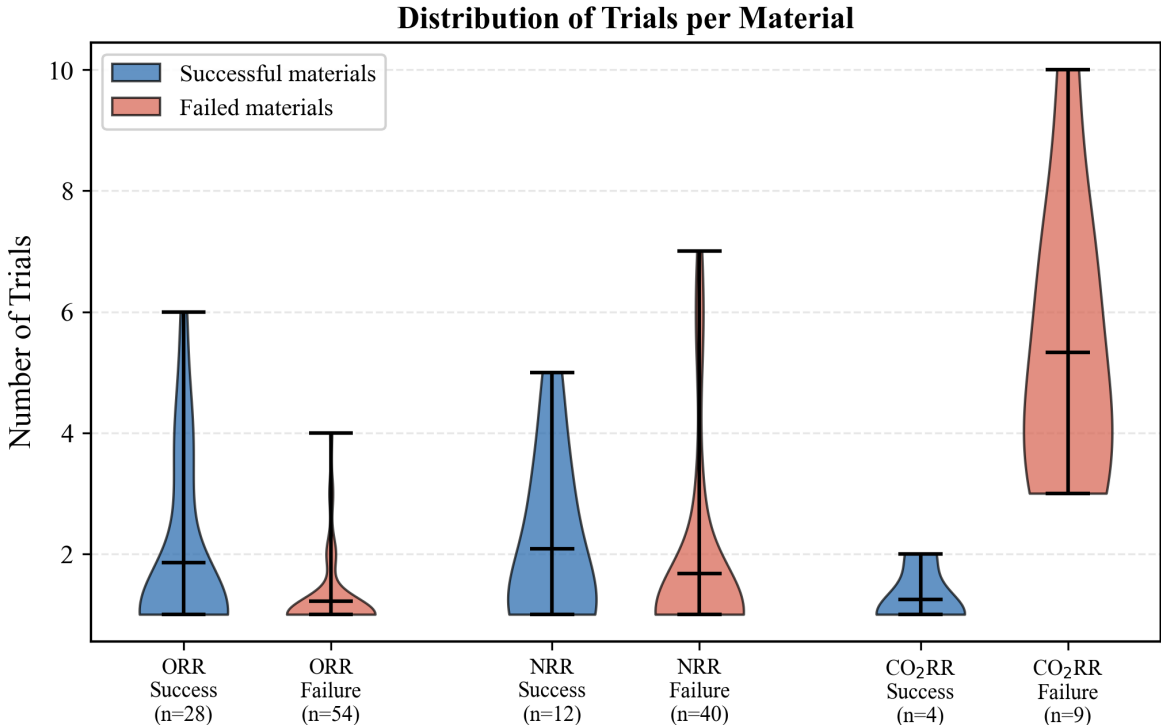


Figure 5: Plots of the number of trials per material, separated by reaction task and outcome category (success vs. failure). Horizontal lines indicate mean and min–max range. The distributions illustrate that convergence is rapid for most successful materials, while a subset of near-miss candidates and most CO₂RR failures require extended iteration.

Overall, these metrics support two complementary conclusions: Catalyst-Agent achieves

nontrivial coverage across diverse electrocatalysis objectives ($R_{\text{succ}} \sim 0.23\text{--}0.34$), and its iterative modification loop is practically efficient, converging in $\sim 1\text{--}2$ trials for successful cases on average. The plots underscore the heterogeneity in both trials-to-success and modification effort: summary means and standard deviations (Tables 3 and 4) are complemented by the full distributions in Figures 3, 4 and 5. The modification-level analysis, restricted to materials that actually entered the refinement loop, reveals that the agent’s surface engineering strategies are most productive when applied to candidates that are already proximate to the descriptor boundary: modified successful materials consistently exhibit a higher ratio of successful to unsuccessful modifications than their modified failure counterparts. Materials that are intrinsically far from the target window accumulate more unsuccessful modification attempts and resist surface-level rescue. The agent is also quite persistent for promising materials that eventually failed, with many trials attempted, especially for the CO_2RR case. These findings suggest that future screening campaigns may benefit from pre-filtering candidates by proximity to descriptor targets before investing modification effort, a heuristic that the agent implicitly approximates through its near-miss detection logic.

2.4 Illustrative example of agentic reasoning: CoGa_2O_4 (mp-765466) for ORR

To illustrate how Catalyst-Agent autonomously reasons through the closed-loop screening and optimization process, we trace the complete decision history for the cobalt gallate spinel CoGa_2O_4 (Ga_2CoO_4 , Materials Project ID mp-765466) in the ORR $\ast\text{OH}$ screening campaign. This example is representative of the agent’s iterative hypothesis–test–revise workflow and highlights how it combines chemical intuition with quantitative feedback from the AdsorbML-UMA pipeline to converge on a successful modification strategy (Figure 6).

Material selection rationale. CoGa_2O_4 is a normal spinel in which Co^{2+} occupies tetrahedral A-sites and Ga^{3+} fills octahedral B-sites. The agent selected it as a candidate because

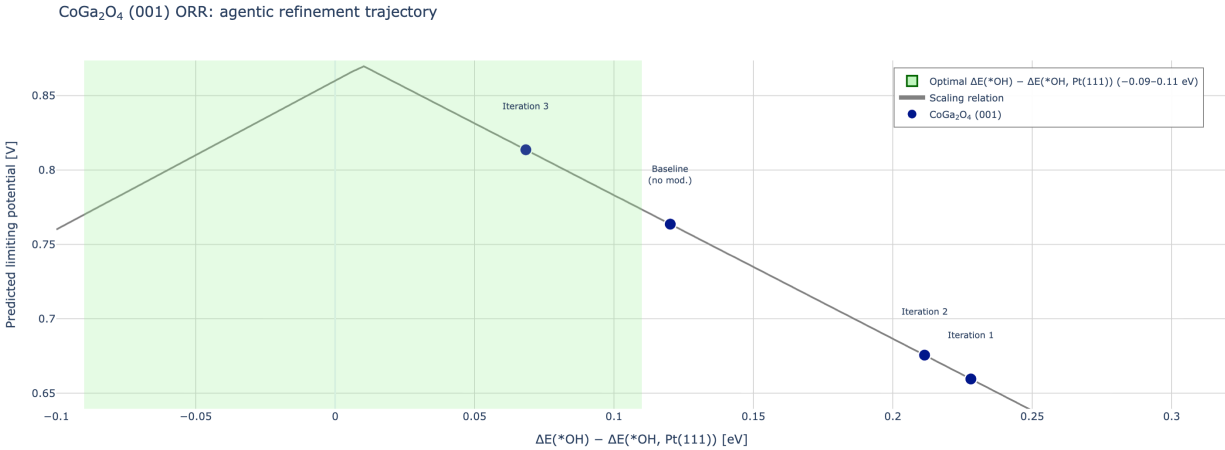


Figure 6: Volcano plot of predicted limiting potential versus $\Delta E(*OH) - \Delta E(*OH, Pt(111))$ for CoGa₂O₄ (001) along the agent’s refinement trajectory. The green band marks the optimal window

of the proven ORR activity of cobalt-based spinels (e.g. Co₃O₄, MgCo₂O₄, CoAl₂O₄) and the opportunity to tune Co–O covalency by substituting the B-site cation (Al \leftrightarrow Ga). The initial baseline evaluation on the unmodified structure returned $E_{\text{ads}}(*OH) = 1.1102$ eV on the (001) facet, placing it barely above the optimal 0.9–1.1 eV target window. This “near-miss” status made CoGa₂O₄ a prime candidate for iterative surface-level refinement.

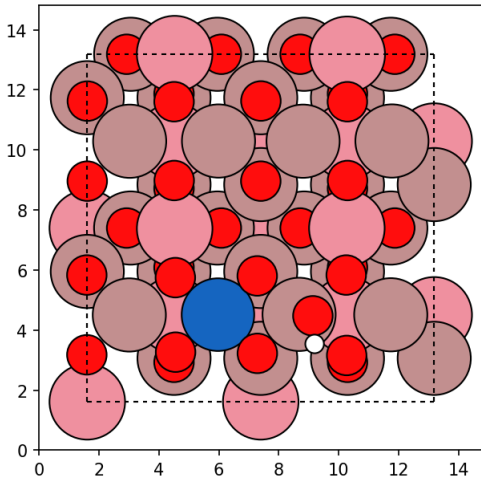


Figure 7: Surface structure illustrating Ga→Al substitution (aluminum atom in blue) with 2% compressive strain, as evaluated in Iteration 1.

Iteration 1 – Ga→Al surface doping with 2% compressive strain: The agent’s first hypothesis was that replacing the surface Ga atom with the more electronegative Al would increase local ionicity and simultaneously applying 2% compressive strain would contract the Co–O bond lengths, together softening the slightly-too-strong *OH binding, as shown in Figure 7. AdsorbML returned $E_{\text{ads}}(*\text{OH})$ values of 1.2180 eV on (001) and 1.2042 eV on (100), both further from the optimal window than the baseline. The remaining facets were either strongly overbinding ((110): -0.6318 eV, (111): -0.8609 eV) or far too weak ((210): 0.0084 eV). The agent concluded that Al substitution combined with compression pushed adsorption in the wrong direction and abandoned this modification.

Iteration 2 – 2% compressive strain only: To disentangle the dopant effect from the strain effect, the agent removed the Al substituent and re-evaluated the surface under 2% compressive strain alone. The (001) facet returned 1.2014 eV and (100) returned 1.1159 eV, both still above the target window, while (111) showed extreme overbinding at -4.4015 eV. The agent inferred that compressive strain, regardless of doping, strengthens rather than softens *OH adsorption on the low-index spinel terminations of CoGa_2O_4 . This observation prompted the agent to reverse its strain strategy.

Iteration 3 – 2% tensile strain only: Having established that compression moves adsorption away from the target, the agent applied 2% tensile strain without any dopant. The (001) facet returned $E_{\text{ads}}(*\text{OH}) = 1.0584$ eV, placing it squarely inside the optimal 0.9–1.1 eV band. The agent successfully identified CoGa_2O_4 (001) under 2% tensile strain as a viable ORR catalyst candidate after a total of four evaluations (one baseline and three modification trials). Figure 6 summarizes this trajectory on a volcano plot obtained from Kulkarni et al.⁷⁰

Modification statistics. Quantitatively, the CoGa_2O_4 screening trajectory comprised a total of four trials: one baseline evaluation followed by three surface modifications. Of

these three modifications, two were classified as successful (the compressive-strain-only trial produced the (100) facet at 1.1159 eV which, while marginally outside the target, moved closer than the combined doping-plus-strain attempt, and the tensile-strain trial placed the (001) facet squarely inside the target window) and one was unsuccessful (the combined Ga→Al doping with compressive strain moved all evaluated facets further from the target). This 2:1 ratio of successful to unsuccessful modifications for CoGa₂O₄ is comparable to the campaign-wide average for modified ORR success materials (1.67 successful vs. 1.00 unsuccessful per material among those entering the modification loop; Table 4), reflecting the particular amenability of the spinel surface to strain-based tuning once the correct sign of the elastic perturbation was identified. In contrast, ORR failure materials that entered the modification loop averaged only 0.50 successful modifications against 1.00 unsuccessful ones: a ratio that is inverted relative to the success cohort, underscoring that surface modifications are substantially more productive when the base material performance is near the descriptor boundary. The four total trials required for CoGa₂O₄ place it above the ORR campaign mean ($\bar{t}_{\text{succ}} = 1.86$), which is expected given that most ORR successes are first-trial hits on the unmodified baseline. The materials that do require modification, as CoGa₂O₄ did, naturally populate the tail of the trial distribution and illustrate the value of the iterative refinement loop for near-miss candidates.

Reasoning summary. The agent’s decision trace for CoGa₂O₄ demonstrates several key aspects of the autonomous reasoning loop:

1. **Chemical hypothesis generation:** The agent drew on spinel crystal-chemistry knowledge to propose both compositional (Ga→Al doping) and mechanical (strain) modifications as plausible tuning strategies.
2. **Systematic isolation of variables:** After the combined doping-plus-strain attempt failed, the agent removed the dopant to isolate the elastic effect, a standard experimental-design principle applied autonomously.

3. **Feedback-driven sign reversal:** The quantitative AdsorbML feedback revealed that compressive strain strengthened adsorption on CoGa_2O_4 , contrary to the initial expectation. The agent reversed the strain direction in the next iteration, demonstrating adaptive reasoning rather than fixed heuristics.
4. **Convergence within few trials:** The agent reached an optimal condition within four evaluations, consistent with the campaign-wide average of $\bar{t}_{\text{succ}} \approx 1.86$ trials for ORR (Table 3).
5. **Efficient modification selection:** Over three modification attempts the agent achieved a 2:1 success-to-failure ratio, consistent with the campaign-wide trend that modified successful materials exhibit more successful than unsuccessful modifications (Table 4).

This example underscores that Catalyst-Agent does not follow a pre-programmed script for surface optimization but instead generates, tests and revises modification hypotheses in real time, guided by physically grounded energy feedback from the AdsorbML–UMA pipeline. The modification statistics for CoGa_2O_4 are consistent with the broader campaign-level trends reported in Table 4: among materials that entered the modification loop, successful materials consistently achieve a higher ratio of successful to unsuccessful modifications than failure materials, demonstrating that the agent’s surface engineering is most productive for near-miss candidates already proximate to the descriptor boundary. The full decision trace is logged in structured JSON; an illustrative example of the complete MCP tool-call sequence for a single material is given in Section S2, and the raw tuning history for CoGa_2O_4 is recorded in Section S3.

Critical assessment of the agent’s reasoning. Despite converging within four trials, the agent’s verbal reasoning systematically inverts thermodynamic language: the positive baseline $E_{\text{ads}} = 1.1102$ eV indicates weak adsorption, yet the agent labeled it “too-strong” binding and aimed to “soften” it. When modifications raised E_{ads} further, the agent correctly

identified these as wrong-direction moves without reconciling this with its own softening objective. Convergence was achieved through accurate numerical tracking of the descriptor rather than physically consistent reasoning. Moreover, the lauded “systematic isolation of variables” in Iteration 2 was a corrective step forced by the agent’s own choice to confound doping and strain in Iteration 1, and the subsequent “sign reversal” of strain direction amounts to exhaustive search over a binary parameter rather than a prediction grounded in electronic-structure reasoning about Co–O covalency or *d*-band shifts. There is trial and error with some limited physical understanding at play here.

3 Challenges and Future Directions

While these case studies showcase the ability of an agent to execute end-to-end adsorption energy calculations for catalytic screening and iterate over user-defined constraints, there are some practical challenges that remain before broad scientific application.

From thermochemical descriptors to operating conditions. This study uses adsorption energies as reaction descriptors, but electrocatalysis involves more variables like the solvent, electrolyte, applied potentials, field effects, surface reconstruction, zero-point energy corrections and competing reaction pathways. Extending this workflow to accommodate coverage dependent adsorption, constant-potential/implicit solvation corrections and microkinetic modeling would help in reinforcing the connection between these descriptors and experimentally accurate and measurable activity/selectivity. Simultaneously integrating stability descriptors such as phase stability and surface segregation would help filter candidates that are thermochemically plausible but experimentally non-viable.

Beyond heuristic refinement operators. The modifications employed in this paper (in-plane strain and single top-layer substitution) provide paths for iterative improvement but they do not span the full space of realistic possible catalyst modifications. Future extensions

could include multi-site atomic substitution, ordered surface alloys, defect creation and strain fields other than uniform biaxial strain.

Hybrid validation loops and human oversight. A practical deployment option is a hybrid pipeline where ML-driven screening gives testable hypotheses, ranks good candidates, while selected finalists are sent over for validation by means of higher-fidelity calculations (example: DFT) and ultimately by experiment. This loop may be modified further by active learning, where high-fidelity results are fed back to update the surrogate model in interesting regions to improve the performance over time. Incorporating "scientist-in-the-loop" interfaces may be beneficial for dynamic constraint settings, interpretability and safe, productive use in a real research environment.

LLM Hallucination bias. The Agent's decisions inherit the limitations of the LLM's hallucinations, planning heuristics and biases in its training data.

4 Conclusions

In this work, we presented Catalyst-Agent, an autonomous, tool-grounded LLM agent that operationalizes catalyst screening workflows as closed-loop processing campaigns. By combining a standardized command-line interface to tools that use the OPTIMADE API for structure retrieval and ML-accelerated adsorption energy evaluation using the UMA-powered AdsorbML pipeline, the agent is able to translate scientific natural language commands and objectives into reproducible sequences of actions: finding candidate materials, slab construction, adsorption energy calculation, constraint evaluation and iterative refinement via simple surface modifications. Across the ORR, NRR and CO₂RR-motivated reaction descriptors, the agent achieved a reasonable success rate across all catalyst candidates and converged to success within $\sim 1-2$ trials when success was possible, illustrating that autonomous processing and iteration can reduce the human researcher's time and effort in computational

catalysis exploration. These results also demonstrate the potential of AI agents for novel catalyst screening and discovery. Notably, the agent identified Sn_3Sc as a potential novel CO_2RR catalyst not previously reported in the literature.

Despite these challenges and limitations, the results support a clear conclusion: LLM-powered agents can be combined with advanced computational scientific tools and can execute end-to-end catalyst screening and iterative optimization with minimal human intervention. From a practical standpoint, the modular MCP server architecture naturally isolates conflicting software dependencies, improving maintainability and extensibility, while the generous free tiers and rate limits of current LLM APIs keep short screening campaigns accessible at negligible cost, though larger-scale campaigns will incur proportionally higher API expenses (token usage and costs are detailed in Section S6). This work creates a practical pathway toward speedy, scalable and reproducible computational discovery loops. Human effort can now be shifted from scripting to defining objectives, high-level orchestration and pattern recognition.

5 Methods

5.1 Surrogate model: UMA small (uma-s-1p1)

Adsorption energy relaxations and computation were carried out using FAIRchem’s pre-trained UMA small model (uma-s-1p1), which was accessed through FAIRchem’s code repository. It was wrapped in an ASE-compatible calculator (FAIRChemCalculator). In this work, UMA serves as a machine learning interatomic potential that calculates energies and forces. General model training and details are described in FAIRchem’s documentation.

5.2 AdsorbML adsorption-energy workflow

Adsorption energies were computed using FAIRchem’s AdsorbML pipeline. For each material-adsorbate system, AdsorbML generates several initial adsorbate placements on the catalyst

slab surface and relaxes each placement using the UMA small model. Referenced adsorption energies are reported with respect to the gas phase adsorbate molecules and the global minimum energy of each configuration is taken as the adsorption energy. Each evaluation returns a detailed summarized result of the number of attempted configurations, the number of valid configurations, the number of configurations with anomalies and the minimum-energy configuration with energy decomposition into clean-slab, gas phase reference and adsorbate-slab totals.

5.3 Model Context Protocol (MCP) tool servers

The agent is augmented with the toolchain infrastructure through five MCP servers created with the help of the Model Context Protocol (MCP) framework.⁴⁶ Subprocess-isolation ensures failures are contained, GPU overloading is avoided and enables structured error reporting. All results are summarized in the JSON format to cater to the agent’s textual understanding.

5.4 LLM agent environment: Codex CLI

Codex CLI was used as the LLM command-line environment for planning and orchestration.⁵⁷ It is an agentic environment, developed by OpenAI, primarily for coding and can be run locally from the terminal. It is open-source software built using the Rust programming language.⁷⁵ Codex CLI was used to run the GPT-5.2 model from OpenAI. This model was chosen for its excellent scientific understanding and reasoning capabilities.

5.5 Devices and Codebase

We deployed the GPT-5.2 model through the Codex Command Line Interface (CLI) from OpenAI.⁵⁷ For public benefit and further research, the code, supplementary information and raw output files are available at the following link: <https://github.com/BaratiLab/>

```
> _ OpenAI Codex (v0.98.0)
model:      gpt-5.2 high  /model to change
directory:  ~/Documents

Tip: New Try the Codex App with 2x rate limits until April 2nd. Run 'codex app' or visit https://chatgpt.com/codex

> Explain this codebase
? for shortcuts                                     100% context left
```

Figure 8: Codex CLI (command-line interface) was used as the GPT-5.2 powered LLM-agent environment and user interface.

Catalyst_agent. All simulations were performed using an NVIDIA A6000 GPU with 48 GB of RAM. LLM API token usage and costs are reported in Section S6.

Acknowledgement

The authors thank Omid Barati, Abraham George, Yayati Jadhav, Radheesh Sharma Meda, and Yue Su for insightful discussions and helpful suggestions. ChatGPT was utilized for grammatical refinement and typographical corrections.

Supporting Information Available

The Supporting Information is available free of charge at: https://github.com/BaratiLab/Catalyst_agent

References

- (1) Nørskov, J. K.; Studt, F.; Abild-Pedersen, F.; Bligaard, T. *Fundamental concepts in heterogeneous catalysis*; John Wiley & Sons, 2014.
- (2) Dumesic, J. A.; Huber, G. W.; Boudart, M. Principles of heterogeneous catalysis. *Handbook of heterogeneous catalysis* **1996**,

- (3) Zitnick, C. L.; Chanussot, L.; Das, A.; Goyal, S.; Heras-Domingo, J.; Ho, C.; Hu, W.; Lavril, T.; Palizhati, A.; Riviere, M.; others An introduction to electrocatalyst design using machine learning for renewable energy storage. *arXiv preprint arXiv:2010.09435* **2020**,
- (4) Raccuglia, P.; Elbert, K. C.; Adler, P. D.; Falk, C.; Wenny, M. B.; Mollo, A.; Zeller, M.; Friedler, S. A.; Schrier, J.; Norquist, A. J. Machine-learning-assisted materials discovery using failed experiments. *Nature* **2016**, *533*, 73–76.
- (5) Wang, H.; Zhao, Y.; Zhang, Z.; Zhu, Y.; Li, X.; Zhang, D. A Density Functional Theory (DFT) Modeling Study of NO Reduction by CO over Graphene-Supported Single-Atom Ni Catalysts in the Presence of CO₂, SO₂, O₂, and H₂O. *Langmuir* **2025**, *41*, 1614–1624.
- (6) Ock, J.; Tian, T.; Kitchin, J.; Ulissi, Z. Beyond independent error assumptions in large GNN atomistic models. *The Journal of Chemical Physics* **2023**, *158*.
- (7) Chen, C.; Li, Z.; Yang, J.; Wang, H.; Chen, D. Descriptor-Driven Prediction of Adsorption Energy of Oxygenates on Metal Dioxide Surfaces. *The Journal of Physical Chemistry C* **2025**, *129*, 6245–6253.
- (8) Karimadom, B. R.; Meyerstein, D.; Kornweitz, H. Calculating the adsorption energy of a charged adsorbent in a periodic metallic system—the case of BH 4- hydrolysis on the Ag (111) surface. *Physical Chemistry Chemical Physics* **2021**, *23*, 25667–25678.
- (9) Ock, J.; Meda, R. S.; Vinchurkar, T.; Jadhav, Y.; Farimani, A. B. Adsorb-Agent: autonomous identification of stable adsorption configurations via a large language model agent. *Digital Discovery* **2026**,
- (10) Lan, J.; Palizhati, A.; Shuaibi, M.; Wood, B. M.; Wander, B.; Das, A.; Uyttendaele, M.; Zitnick, C. L.; Ulissi, Z. W. AdsorbML: a leap in efficiency for adsorption energy cal-

- culations using generalizable machine learning potentials. *npj Computational Materials* **2023**, *9*, 172.
- (11) Chen, J.; Huang, X.; Hua, C.; He, Y.; Schwaller, P. A multi-modal transformer for predicting global minimum adsorption energy. *Nature Communications* **2025**, *16*, 3232.
- (12) Klawohn, S.; Darby, J. P.; Kermode, J. R.; Csányi, G.; Caro, M. A.; Bartók, A. P. Gaussian approximation potentials: Theory, software implementation and application examples. *The Journal of Chemical Physics* **2023**, *159*.
- (13) Kÿvala, L.; Dellago, C. Optimizing the architecture of Behler–Parrinello neural network potentials. *The Journal of Chemical Physics* **2023**, *159*.
- (14) Srinivasan, P.; Demuriya, D.; Grabowski, B.; Shapeev, A. Electronic Moment Tensor Potentials include both electronic and vibrational degrees of freedom. *npj Computational Materials* **2024**, *10*, 41.
- (15) Li, H.; Wang, Z.; Zou, N.; Ye, M.; Xu, R.; Gong, X.; Duan, W.; Xu, Y. Deep-learning density functional theory Hamiltonian for efficient ab initio electronic-structure calculation. *Nature Computational Science* **2022**, *2*, 367–377.
- (16) Thant, Y. M.; Wakamiya, T.; Nukunudompanich, M.; Kameda, K.; Ihara, M.; Manzhos, S. Kernel regression methods for prediction of materials properties: Recent developments. *Chemical Physics Reviews* **2025**, *6*.
- (17) Pun, G. P.; Batra, R.; Ramprasad, R.; Mishin, Y. Physically informed artificial neural networks for atomistic modeling of materials. *Nature communications* **2019**, *10*, 2339.
- (18) Cao, Z.; Barati Farimani, O.; Ock, J.; Barati Farimani, A. Machine learning in membrane design: from property prediction to AI-guided optimization. *Nano letters* **2024**, *24*, 2953–2960.

- (19) Deng, B.; Zhong, P.; Jun, K.; Riebesell, J.; Han, K.; Bartel, C. J.; Ceder, G. CHGNet as a pretrained universal neural network potential for charge-informed atomistic modelling. *Nature Machine Intelligence* **2023**, *5*, 1031–1041.
- (20) Liao, Y.-L.; Wood, B.; Das, A.; Smidt, T. Equiformerv2: Improved equivariant transformer for scaling to higher-degree representations. *arXiv preprint arXiv:2306.12059* **2023**,
- (21) Batzner, S.; Musaelian, A.; Sun, L.; Geiger, M.; Mailoa, J. P.; Kornbluth, M.; Molinari, N.; Smidt, T. E.; Kozinsky, B. E (3)-equivariant graph neural networks for data-efficient and accurate interatomic potentials. *Nature communications* **2022**, *13*, 2453.
- (22) Batatia, I.; Kovacs, D. P.; Simm, G.; Ortner, C.; Csányi, G. MACE: Higher order equivariant message passing neural networks for fast and accurate force fields. *Advances in neural information processing systems* **2022**, *35*, 11423–11436.
- (23) Choudhary, K.; DeCost, B. Atomistic line graph neural network for improved materials property predictions. *npj Computational Materials* **2021**, *7*, 185.
- (24) Chen, C.; Ye, W.; Zuo, Y.; Zheng, C.; Ong, S. P. Graph networks as a universal machine learning framework for molecules and crystals. *Chemistry of Materials* **2019**, *31*, 3564–3572.
- (25) Wood, B. M.; Dzamba, M.; Fu, X.; Gao, M.; Shuaibi, M.; Barroso-Luque, L.; Abdelmaqsoud, K.; Gharakhanyan, V.; Kitchin, J. R.; Levine, D. S.; others UMA: A Family of Universal Models for Atoms. *arXiv preprint arXiv:2506.23971* **2025**,
- (26) Kabylda, A.; Frank, J.; Dou, S.; Khabibrakhmanov, A.; Sandonas, L.; Unke, O.; Chmiela, S.; Muller, K.; Tkatchenko, A. Molecular Simulations with a Pretrained Neural Network and Universal Pairwise Force Fields (2025).

- (27) Maheshwari, S.; Tang, Z.; Ock, J.; Kolluru, A.; Farimani, A. B.; Kitchin, J. R. Beyond Force Metrics: Pre-Training MLFFs for Stable MD Simulations. *arXiv preprint arXiv:2506.14850* **2025**,
- (28) Han, K.; Deng, B.; Farimani, A. B.; Ceder, G. Distmlip: A distributed inference platform for machine learning interatomic potentials. *arXiv preprint arXiv:2506.02023* **2025**,
- (29) Shuaibi, M. et al. FAIRChem. <https://github.com/facebookresearch/fairchem>.
- (30) Vaswani, A.; Shazeer, N.; Parmar, N.; Uszkoreit, J.; Jones, L.; Gomez, A. N.; Kaiser, Ł.; Polosukhin, I. Attention is all you need. *Advances in neural information processing systems* **2017**, *30*.
- (31) Chaudhari, A.; Guntuboina, C.; Huang, H.; Farimani, A. B. AlloyBERT: Alloy property prediction with large language models. *Computational Materials Science* **2024**, *244*, 113256.
- (32) Jadhav, Y.; Pak, P.; Farimani, A. B. Llm-3D print: large language models to monitor and control 3D printing. *Additive Manufacturing* **2025**, 105027.
- (33) Badrinarayanan, S.; Magar, R.; Antony, A.; Meda, R. S.; Barati Farimani, A. MOFGPT: Generative design of metal–organic frameworks using language models. *Journal of Chemical Information and Modeling* **2025**, *65*, 9049–9060.
- (34) Chandrasekhar, A.; Farimani, O. B.; Ajenifujah, O. T.; Ock, J.; Farimani, A. B. NANOGPT: a query-driven large language model retrieval-augmented generation system for nanotechnology research. *arXiv preprint arXiv:2502.20541* **2025**,
- (35) Chandrasekhar, A.; Chan, J.; Ogoke, F.; Ajenifujah, O.; Farimani, A. B. AMGPT: A large language model for contextual querying in additive manufacturing. *Additive Manufacturing Letters* **2024**, *11*, 100232.

- (36) Ock, J.; Guntuboina, C.; Barati Farimani, A. Catalyst Energy Prediction with CatBERTa: Unveiling Feature Exploration Strategies through Large Language Models. *ACS Catalysis* **2023**, *13*, 16032–16044.
- (37) Wang, Y.; Wang, J.; Cao, Z.; Barati Farimani, A. Molecular contrastive learning of representations via graph neural networks. *Nature Machine Intelligence* **2022**, *4*, 279–287.
- (38) Mok, D. H.; Back, S. Generative pretrained transformer for heterogeneous catalysts. *Journal of the American Chemical Society* **2024**, *146*, 33712–33722.
- (39) Radford, A.; Wu, J.; Child, R.; Luan, D.; Amodei, D.; Sutskever, I.; others Language models are unsupervised multitask learners. *OpenAI blog* **2019**, *1*, 9.
- (40) Devlin, J.; Chang, M.-W.; Lee, K.; Toutanova, K. Bert: Pre-training of deep bidirectional transformers for language understanding. Proceedings of the 2019 conference of the North American chapter of the association for computational linguistics: human language technologies, volume 1 (long and short papers). 2019; pp 4171–4186.
- (41) Sprueill, H. W.; Edwards, C.; Agarwal, K.; Olarte, M. V.; Sanyal, U.; Johnston, C.; Liu, H.; Ji, H.; Choudhury, S. ChemReasoner: Heuristic search over a large language model’s knowledge space using quantum-chemical feedback. *arXiv preprint arXiv:2402.10980* **2024**,
- (42) Achiam, J.; Adler, S.; Agarwal, S.; Ahmad, L.; Akkaya, I.; Aleman, F. L.; Almeida, D.; Altschmidt, J.; Altman, S.; Anadkat, S.; others Gpt-4 technical report. *arXiv preprint arXiv:2303.08774* **2023**,
- (43) Yao, T.; Yang, Y.; Cai, J.; Liu, R.; Dong, Z.; Tang, X.; Shao, X.; Gao, Z.; An, G.; Yang, W. From LLM to agent: a large-language-model-driven machine learning framework for catalyst design of MgH₂ dehydrogenation. *Journal of Magnesium and Alloys* **2025**,

- (44) Ye, Q.; Ahmed, M.; Pryzant, R.; Khani, F. Prompt engineering a prompt engineer. Findings of the Association for Computational Linguistics: ACL 2024. 2024; pp 355–385.
- (45) Lundberg, S. M.; Lee, S.-I. A unified approach to interpreting model predictions. *Advances in neural information processing systems* **2017**, *30*.
- (46) Introducing the Model Context Protocol. <https://www.anthropic.com/news/model-context-protocol>.
- (47) Nigam, V.; Chandrasekhar, A.; Farimani, A. B. Polymer-Agent: Large Language Model Agent for Polymer Design. 2026; <https://arxiv.org/abs/2601.16376>.
- (48) Pak, P.; Chandrasekhar, A.; Farimani, A. B. Agentic additive manufacturing alloy evaluation. *Additive Manufacturing Letters* **2026**, 100355.
- (49) Jadhav, Y.; Barati Farimani, A. Large language model agent as a mechanical designer. *Journal of Engineering Design* **2026**, 1–37.
- (50) Zeng, T.; Badrinarayanan, S.; Ock, J.; Lai, C.-K.; Barati Farimani, A. LLM-guided chemical process optimization with a multi-agent approach. *Machine Learning: Science and Technology* **2025**, *6*, 045067.
- (51) Han, K.; Maddikayala, S.; Knappe, T.; Patel, O.; Liao, A.; Barati Farimani, A. TDFlow: Agentic Workflows for Test Driven Software Engineering. *arXiv e-prints* **2025**, arXiv–2510.
- (52) Ock, J.; Meda, R. S.; Badrinarayanan, S.; Aluru, N. S.; Chandrasekhar, A.; Barati Farimani, A. Large language model agent for modular task execution in drug discovery. *Journal of Chemical Information and Modeling* **2025**,
- (53) Chandrasekhar, A.; Farimani, A. Automating MD simulations for Proteins using Large language Models: NAMD-Agent. 2025.

- (54) Chaudhari, A.; Ock, J.; Barati Farimani, A. Modular large language model agents for multi-task computational materials science. **2025**,
- (55) Ghafarollahi, A.; Buehler, M. J. Rapid and automated alloy design with graph neural network-powered large language model-driven multi-agent AI. *MRS Bulletin* **2025**, *50*, 1309–1324.
- (56) Wang, F. Y.; Lee, D. S.; Kaplan, D. L.; Buehler, M. J. Swarms of Large Language Model Agents for Protein Sequence Design with Experimental Validation. *arXiv preprint arXiv:2511.22311* **2025**,
- (57) OpenAI Codex CLI. <https://developers.openai.com/codex/cli/>, 2025; <https://developers.openai.com/codex/cli/>, Accessed: 2026-01-30.
- (58) Perplexity Team Introducing Perplexity Deep Research. 2025; <https://www.perplexity.ai/hub/blog/introducing-perplexity-deep-research>.
- (59) Winther, K. T.; Hoffmann, M. J.; Boes, J. R.; Mamun, O.; Bajdich, M.; Bligaard, T. Catalysis-Hub.org, an open electronic structure database for surface reactions. *Scientific data* **2019**, *6*, 75.
- (60) Andersen, C. W.; Armiento, R.; Blokhin, E.; Conduit, G. J.; Dwaraknath, S.; Evans, M. L.; Fekete, Á.; Gopakumar, A.; Gražulis, S.; Merkys, A.; others OPTI-MADE, an API for exchanging materials data. *Scientific data* **2021**, *8*, 217.
- (61) Jain, A.; Ong, S. P.; Hautier, G.; Chen, W.; Richards, W. D.; Dacek, S.; Cholia, S.; Gunter, D.; Skinner, D.; Ceder, G.; others Commentary: The Materials Project: A materials genome approach to accelerating materials innovation. *APL materials* **2013**, *1*.
- (62) Saal, J. E.; Kirklin, S.; Aykol, M.; Meredig, B.; Wolverton, C. Materials design and

- discovery with high-throughput density functional theory: the open quantum materials database (OQMD). *Jom* **2013**, *65*, 1501–1509.
- (63) Kirklin, S.; Saal, J. E.; Meredig, B.; Thompson, A.; Doak, J. W.; Aykol, M.; Rühl, S.; Wolverton, C. The Open Quantum Materials Database (OQMD): assessing the accuracy of DFT formation energies. *npj Computational Materials* **2015**, *1*, 1–15.
- (64) Gražulis, S.; Daškevič, A.; Merkys, A.; Chateigner, D.; Lutterotti, L.; Quiros, M.; Serebryanaya, N. R.; Moeck, P.; Downs, R. T.; Le Bail, A. Crystallography Open Database (COD): an open-access collection of crystal structures and platform for world-wide collaboration. *Nucleic acids research* **2012**, *40*, D420–D427.
- (65) Ong, S. P.; Richards, W. D.; Jain, A.; Hautier, G.; Kocher, M.; Cholia, S.; Gunter, D.; Chevrier, V. L.; Persson, K. A.; Ceder, G. Python Materials Genomics (pymatgen): A robust, open-source python library for materials analysis. *Computational Materials Science* **2013**, *68*, 314–319.
- (66) Larsen, A. H.; Mortensen, J. J.; Blomqvist, J.; Castelli, I. E.; Christensen, R.; Dułak, M.; Friis, J.; Groves, M. N.; Hammer, B.; Hargus, C.; others The atomic simulation environment—a Python library for working with atoms. *Journal of Physics: Condensed Matter* **2017**, *29*, 273002.
- (67) Hall, S. R.; Allen, F. H.; Brown, I. D. The crystallographic information file (CIF): a new standard archive file for crystallography. *Foundations of Crystallography* **1991**, *47*, 655–685.
- (68) Sun, J.; Tu, R.; Xu, Y.; Yang, H.; Yu, T.; Zhai, D.; Ci, X.; Deng, W. Machine learning aided design of single-atom alloy catalysts for methane cracking. *Nature Communications* **2024**, *15*, 6036.
- (69) Oliveira, C. C.; Autreto, P. A. Strain-Engineered Jacutingaite Analogs as Efficient 2D Catalysts for Hydrogen Evolution Reactions. *ACS omega* **2025**, *10*, 59469–59477.

- (70) Kulkarni, A.; Siahrostami, S.; Patel, A.; Nørskov, J. K. Understanding catalytic activity trends in the oxygen reduction reaction. *Chemical reviews* **2018**, *118*, 2302–2312.
- (71) Man, I. C.; Su, H.-Y.; Calle-Vallejo, F.; Hansen, H. A.; Martínez, J. I.; Inoglu, N. G.; Kitchin, J.; Jaramillo, T. F.; Nørskov, J. K.; Rossmeisl, J. Universality in oxygen evolution electrocatalysis on oxide surfaces. *ChemCatChem* **2011**, *3*, 1159–1165.
- (72) Wang, Y.; Cheng, H.-P. Oxygen reduction activity on perovskite oxide surfaces: a comparative first-principles study of LaMnO₃, LaFeO₃, and LaCrO₃. *The Journal of Physical Chemistry C* **2013**, *117*, 2106–2112.
- (73) Song, Z.; Fan, L.; Lu, S.; Ling, C.; Zhou, Q.; Wang, J. Inverse design of promising electrocatalysts for CO₂ reduction via generative models and bird swarm algorithm. *Nature Communications* **2025**, *16*, 1053.
- (74) Araujo, R. B.; Pehlivan, I. B.; Edvinsson, T. High-entropy alloy catalysts: Fundamental aspects, promises towards electrochemical NH₃ production, and lessons to learn from deep neural networks. *Nano Energy* **2023**, *105*, 108027.
- (75) Bugden, W.; Alahmar, A. Rust: The programming language for safety and performance. *arXiv preprint arXiv:2206.05503* **2022**,
- (76) Chanussot, L.; Das, A.; Goyal, S.; Lavril, T.; Shuaibi, M.; Riviere, M.; Tran, K.; Heras-Domingo, J.; Ho, C.; Hu, W.; others Open catalyst 2020 (OC20) dataset and community challenges. *Acs Catalysis* **2021**, *11*, 6059–6072.
- (77) Gasteiger, J.; Shuaibi, M.; Sriram, A.; Günnemann, S.; Ulissi, Z.; Zitnick, C. L.; Das, A. GemNet-OC: developing graph neural networks for large and diverse molecular simulation datasets. *arXiv preprint arXiv:2204.02782* **2022**,

Supplemental Information

S1 Example User Prompt: ORR Screening with Iterative Modification

The following is a representative user prompt submitted to Catalyst-Agent for an end-to-end ORR screening campaign. This prompt demonstrates how a researcher specifies the target reaction, adsorbate, acceptance criteria, tool-server routing and iterative modification strategy in natural language. The agent parses these instructions and autonomously plans the sequence of MCP tool calls required to execute the screening workflow.

```
Use the perplexity mcp server to get a list of good candidates
for the oxygen reduction reaction. Use the structure retrieval
mcp server to get the pymatgen structures. Run the energy
evaluation server using the *OH adsorbate. The ideal energy
should be between 0.9-1.1 eV. You may apply modifications using
the structure modification mcp server after trying a run with
no modifications. Please search and run one material at a time.
```

This prompt encodes several operational directives that the agent decomposes into discrete planning steps:

1. **Candidate sourcing:** The Catalyst Information Server (backed by Perplexity Deep Research) is queried first to obtain a literature-informed list of promising oxide compositions for ORR.
2. **Structure retrieval:** For each candidate, the Structure Retrieval Server queries the OPTIMADE API to obtain serialized pymatgen structure objects from the Materials Project and OQMD.
3. **Baseline evaluation:** The Energy Evaluation Server computes *OH adsorption energies on multiple Miller-index facets using the AdsorbML-UMA pipeline, with the target descriptor window set to 0.9–1.1 eV.

4. **Conditional modification:** Only after an unmodified baseline run does the agent invoke the Structure Modification Server to apply strain or top-layer substitution, guided by the energetic feedback from the baseline.
5. **Sequential processing:** The instruction to “search and run one material at a time” directs the agent to complete the full evaluate–modify–re-evaluate loop for each candidate before proceeding to the next, ensuring that context-window usage remains manageable and that per-material decision traces are cleanly separated.

The screening results produced from this class of prompt are reported in Tables 5–6 (raw output) and Tables 11–12 (human-ranked outcomes).

S2 Example MCP Tool Calls: CoAl_2O_4 (mp-36447)

This section presents the complete sequence of MCP tool calls executed by Catalyst-Agent during the screening of CoAl_2O_4 (Materials Project identifier mp-36447, spacegroup $Fd\bar{3}m$) for the oxygen reduction reaction using the *OH adsorbate. Each call is shown with its tool name, input parameters (JSON), and the returned output (JSON). The outer MCP protocol envelope (`"result": "..."`) is unwrapped for clarity; only the parsed payload is shown. Calls 1–5 correspond to structure retrieval and unstrained adsorption energy evaluations across five Miller index facets. Calls 6–9 repeat the adsorption analysis on the same facets under 2% compressive in-plane strain. All energies are in eV.

S2.1 Call 1: Structure Search via OPTIMADE

Tool: `optimade_structure_search`

Input:

```
{
  "elements": ["Co", "Al", "O"],
  "nelements": 3
}
```

Output (truncated; 49 structures returned across Materials Project and OQMD):

```
{
  "message": "Found 49 structures matching criteria",
  "results_summary": [
    {
      "provider": "mp",
      "identifier": "mp-1435808",
      "formula": "AlCoO3",
      "spacegroup": "Pm-3m"
    },
    {
      "provider": "mp",
      "identifier": "mp-1391681",
      "formula": "Al(CoO2)2",
      "spacegroup": "C2/c"
    },
    {
      "provider": "mp",
      "identifier": "mp-36447",
      "formula": "Al2CoO4",
      "spacegroup": "Fd-3m"
    },
    {
      "provider": "oqmd",
      "identifier": 4864833,
      "formula": "Al2CoO4",
      "spacegroup": "Fd-3m"
    }
  ],
  "files_saved": [
    "results.json",
    "results_short.json"
  ]
}
```

The full output includes 28 entries from the Materials Project and 21 from OQMD, spanning formulas AlCoO_3 , $\text{Al}(\text{CoO}_2)_2$, Al_2CoO_4 , $\text{Al}_2\text{Co}_2\text{O}_7$, $\text{Al}_4(\text{CoO}_4)_3$, $\text{Al}_5(\text{CoO}_4)_3$, $\text{Al}(\text{CoO}_2)_3$, and $\text{Al}_2\text{Co}_2\text{O}_5$. The agent selected mp-36447 (Al_2CoO_4 , $Fd\bar{3}m$) for subsequent adsorption analysis.

S2.2 Calls 2–5: *OH Adsorption Energy (Unstrained)

The following four calls evaluate *OH adsorption energies on mp-36447 across five Miller index facets without surface modifications. Call 2 evaluates two facets in a single invocation; Calls 3–5 each evaluate one facet.

Call 2: (001) and (100) facets. Tool: adsorbml_analysis

Input:

```
{
  "provider": "mp",
  "identifier": "mp-36447",
  "adsorbate": "*OH",
  "hk1": "[0,0,1]",
  "hk2": "[1,0,0]"
}
```

Output:

```
{
  "provider": "mp",
  "identifier": "mp-36447",
  "adsorbate": "*OH",
  "cif_path": null,
  "doping": null,
  "strain": null,
  "results_by_hkl": {
    "(0,0,1)": {
      "provider": "mp",
      "identifier": "mp-36447",
      "formula": "Al2Co4",
      "spacegroup": "Fd-3m",
      "spacegroup_number": null,
      "adsorbate": "*OH",
      "hkl": [0, 0, 1],
      "cif_path": null,
      "modifications_applied": null,
      "analysis_summary": {
        "total_configurations": 30,
        "valid_configurations": 28,

```

```

    "anomalies_detected": 3
  },
  "minimum_energy_results": {
    "config_index": 0,
    "adsorption_energy": 1.12311411448532,
    "slab_energy": -722.0156515494343,
    "gas_reactant_energy": -10.681,
    "adslab_energy": -731.573537434949
  }
},
"(1,0,0)": {
  "provider": "mp",
  "identifier": "mp-36447",
  "formula": "Al2CoO4",
  "spacegroup": "Fd-3m",
  "spacegroup_number": null,
  "adsorbate": "*OH",
  "hkl": [1, 0, 0],
  "cif_path": null,
  "modifications_applied": null,
  "analysis_summary": {
    "total_configurations": 30,
    "valid_configurations": 26,
    "anomalies_detected": 4
  },
  "minimum_energy_results": {
    "config_index": 0,
    "adsorption_energy": 1.1236939484699224,
    "slab_energy": -722.0156973258015,
    "gas_reactant_energy": -10.681,
    "adslab_energy": -731.5730033773316
  }
}
}
}
}

```

Call 3: (110) facet. Tool: adsorbml_analysis

Input:

```
{
```

```
"provider": "mp",
"identifier": "mp-36447",
"adsorbate": "*OH",
"hkl1": "[1,1,0]"
}
```

Output:

```
{
  "provider": "mp",
  "identifier": "mp-36447",
  "adsorbate": "*OH",
  "cif_path": null,
  "doping": null,
  "strain": null,
  "results_by_hkl": {
    "(1,1,0)": {
      "provider": "mp",
      "identifier": "mp-36447",
      "formula": "Al2Co04",
      "spacegroup": "Fd-3m",
      "spacegroup_number": null,
      "adsorbate": "*OH",
      "hkl": [1, 1, 0],
      "cif_path": null,
      "modifications_applied": null,
      "analysis_summary": {
        "total_configurations": 30,
        "valid_configurations": 20,
        "anomalies_detected": 10
      },
      "minimum_energy_results": {
        "config_index": 0,
        "adsorption_energy": -1.3793883269203615,
        "slab_energy": -722.2220266715051,
        "gas_reactant_energy": -10.681,
        "adslab_energy": -734.2824149984255
      }
    }
  }
}
```

Call 4: (111) facet. Tool: adsorbml_analysis

Input:

```
{
  "provider": "mp",
  "identifier": "mp-36447",
  "adsorbate": "*OH",
  "hkl1": "[1,1,1]"
}
```

Output:

```
{
  "provider": "mp",
  "identifier": "mp-36447",
  "adsorbate": "*OH",
  "cif_path": null,
  "doping": null,
  "strain": null,
  "results_by_hkl": {
    "(1,1,1)": {
      "provider": "mp",
      "identifier": "mp-36447",
      "formula": "Al2CoO4",
      "spacegroup": "Fd-3m",
      "spacegroup_number": null,
      "adsorbate": "*OH",
      "hkl": [1, 1, 1],
      "cif_path": null,
      "modifications_applied": null,
      "analysis_summary": {
        "total_configurations": 30,
        "valid_configurations": 29,
        "anomalies_detected": 1
      },
      "minimum_energy_results": {
        "config_index": 0,
        "adsorption_energy": -4.679040426530305,
        "slab_energy": -1058.8612306200491,
        "gas_reactant_energy": -10.681,
        "adslab_energy": -1074.2212710465794
      }
    }
  }
}
```

```
}  
}  
}  
}
```

Call 5: (210) facet. Tool: adsorbml_analysis

Input:

```
{  
  "provider": "mp",  
  "identifier": "mp-36447",  
  "adsorbate": "*OH",  
  "hkl1": "[2,1,0]"  
}
```

Output:

```
{  
  "provider": "mp",  
  "identifier": "mp-36447",  
  "adsorbate": "*OH",  
  "cif_path": null,  
  "doping": null,  
  "strain": null,  
  "results_by_hkl": {  
    "(2,1,0)": {  
      "provider": "mp",  
      "identifier": "mp-36447",  
      "formula": "Al2Co04",  
      "spacegroup": "Fd-3m",  
      "spacegroup_number": null,  
      "adsorbate": "*OH",  
      "hkl": [2, 1, 0],  
      "cif_path": null,  
      "modifications_applied": null,  
      "analysis_summary": {  
        "total_configurations": 30,  
        "valid_configurations": 26,  
        "anomalies_detected": 4  
      },  
    },  
  },  
}
```

```

    "minimum_energy_results": {
      "config_index": 0,
      "adsorption_energy": -0.5089964812168954,
      "slab_energy": -542.2962311547523,
      "gas_reactant_energy": -10.681,
      "adslab_energy": -553.4862276359692
    }
  }
}
}

```

S2.3 Calls 6–9: *OH Adsorption Energy (2% Compressive Strain)

The following four calls repeat the adsorption analysis on the same facets with 2% compressive in-plane strain applied ($\varepsilon = 0.02$; the a and b lattice vectors are scaled by $1 - \varepsilon$). The `modifications_applied` field in each facet result now records the applied strain.

Call 6: (001) and (100) facets, 2% strain. Tool: adsorbml_analysis

Input:

```

{
  "provider": "mp",
  "identifier": "mp-36447",
  "adsorbate": "*OH",
  "strain": "0.02",
  "hk11": "[0,0,1]",
  "hk12": "[1,0,0]"
}

```

Output:

```

{
  "provider": "mp",
  "identifier": "mp-36447",
  "adsorbate": "*OH",
  "cif_path": null,
  "doping": null,
  "strain": 0.02,

```

```

"results_by_hkl": {
  "(0,0,1)": {
    "provider": "mp",
    "identifier": "mp-36447",
    "formula": "Al2Co04",
    "spacegroup": "Fd-3m",
    "spacegroup_number": null,
    "adsorbate": "*OH",
    "hkl": [0, 0, 1],
    "cif_path": null,
    "modifications_applied": {
      "strain": {
        "value": 0.02,
        "percentage": 2.0,
        "type": "compressive"
      }
    },
    "analysis_summary": {
      "total_configurations": 30,
      "valid_configurations": 24,
      "anomalies_detected": 6
    },
    "minimum_energy_results": {
      "config_index": 0,
      "adsorption_energy": 1.0919098908526212,
      "slab_energy": -720.5685842886923,
      "gas_reactant_energy": -10.681,
      "adslab_energy": -730.1576743978396
    }
  },
  "(1,0,0)": {
    "provider": "mp",
    "identifier": "mp-36447",
    "formula": "Al2Co04",
    "spacegroup": "Fd-3m",
    "spacegroup_number": null,
    "adsorbate": "*OH",
    "hkl": [1, 0, 0],
    "cif_path": null,
    "modifications_applied": {
      "strain": {

```

```

    "value": 0.02,
    "percentage": 2.0,
    "type": "compressive"
  }
},
"analysis_summary": {
  "total_configurations": 30,
  "valid_configurations": 29,
  "anomalies_detected": 1
},
"minimum_energy_results": {
  "config_index": 0,
  "adsorption_energy": 1.0919251496413427,
  "slab_energy": -720.5685842886919,
  "gas_reactant_energy": -10.681,
  "adslab_energy": -730.1576591390506
}
}
}
}

```

Call 7: (110) facet, 2% strain. Tool: adsorbml_analysis

Input:

```

{
  "provider": "mp",
  "identifier": "mp-36447",
  "adsorbate": "*OH",
  "strain": "0.02",
  "hk11": "[1,1,0]"
}

```

Output:

```

{
  "provider": "mp",
  "identifier": "mp-36447",
  "adsorbate": "*OH",
  "cif_path": null,
  "doping": null,

```

```

"strain": 0.02,
"results_by_hkl": {
  "(1,1,0)": {
    "provider": "mp",
    "identifier": "mp-36447",
    "formula": "Al2CoO4",
    "spacegroup": "Fd-3m",
    "spacegroup_number": null,
    "adsorbate": "*OH",
    "hkl": [1, 1, 0],
    "cif_path": null,
    "modifications_applied": {
      "strain": {
        "value": 0.02,
        "percentage": 2.0,
        "type": "compressive"
      }
    },
    "analysis_summary": {
      "total_configurations": 30,
      "valid_configurations": 27,
      "anomalies_detected": 3
    },
    "minimum_energy_results": {
      "config_index": 0,
      "adsorption_energy": -1.4725890105157031,
      "slab_energy": -719.4819296256057,
      "gas_reactant_energy": -10.681,
      "adslab_energy": -731.6355186361214
    }
  }
}
}

```

Call 8: (111) facet, 2% strain. Tool: adsorbml_analysis

Input:

```

{
  "provider": "mp",
  "identifier": "mp-36447",

```

```
"adsorbate": "*OH",
"strain": "0.02",
"hkl1": "[1,1,1]"
}
```

Output:

```
{
  "provider": "mp",
  "identifier": "mp-36447",
  "adsorbate": "*OH",
  "cif_path": null,
  "doping": null,
  "strain": 0.02,
  "results_by_hkl": {
    "(1,1,1)": {
      "provider": "mp",
      "identifier": "mp-36447",
      "formula": "Al2Co04",
      "spacegroup": "Fd-3m",
      "spacegroup_number": null,
      "adsorbate": "*OH",
      "hkl": [1, 1, 1],
      "cif_path": null,
      "modifications_applied": {
        "strain": {
          "value": 0.02,
          "percentage": 2.0,
          "type": "compressive"
        }
      }
    },
    "analysis_summary": {
      "total_configurations": 30,
      "valid_configurations": 30,
      "anomalies_detected": 0
    },
    "minimum_energy_results": {
      "config_index": 0,
      "adsorption_energy": -3.987527365007095,
      "slab_energy": -1055.4064118944632,
      "gas_reactant_energy": -10.681,

```

```
    "adslab_energy": -1070.0749392594703
  }
}
}
```

Call 9: (210) facet, 2% strain. Tool: adsorbml_analysis

Input:

```
{
  "provider": "mp",
  "identifier": "mp-36447",
  "adsorbate": "*OH",
  "strain": "0.02",
  "hkl1": "[2,1,0]"
}
```

Output:

```
{
  "provider": "mp",
  "identifier": "mp-36447",
  "adsorbate": "*OH",
  "cif_path": null,
  "doping": null,
  "strain": 0.02,
  "results_by_hkl": {
    "(2,1,0)": {
      "provider": "mp",
      "identifier": "mp-36447",
      "formula": "Al2Co04",
      "spacegroup": "Fd-3m",
      "spacegroup_number": null,
      "adsorbate": "*OH",
      "hkl": [2, 1, 0],
      "cif_path": null,
      "modifications_applied": {
        "strain": {
          "value": 0.02,
          "percentage": 2.0,

```

```
    "type": "compressive"
  }
},
"analysis_summary": {
  "total_configurations": 30,
  "valid_configurations": 24,
  "anomalies_detected": 6
},
"minimum_energy_results": {
  "config_index": 0,
  "adsorption_energy": -0.6058897917651347,
  "slab_energy": -540.8192414086575,
  "gas_reactant_energy": -10.681,
  "adslab_energy": -552.1061312004226
}
}
}
}
```

S3 Raw Agent Output by Reaction

This section presents the complete raw screening output produced by Catalyst-Agent for each of the three target reactions. Materials are classified into proximity bands relative to the target descriptor window: *Optimal* (within the target), *Close* (within an extended window), *Near* (within a broad window), and *Away* (outside all bands). Tuning histories record every strain and surface-substitution trial attempted by the agent on promising candidates.

S3.1 ORR: *OH Adsorption Energies

The agent screened oxide materials for the oxygen reduction reaction using $E_{\text{ads}}(*\text{OH})$ as the primary descriptor. The target window is 0.9–1.1 eV, with broader bands at 0.8–1.2 eV (Close) and 0.7–1.3 eV (Near). Table 5 lists all materials whose best facet fell within the Optimal, Close, or Near bands. Each entry records only the facet that achieved the best-band classification for that material. Five adsorbate placements were used per facet in the initial screening round and thirty placements in the second round.

Table 5: Raw agent *OH adsorption energies for ORR screening—Optimal, Close, and Near band entries. Energies in eV.

Material	Identifier	Facet	$E_{\text{ads}}(*\text{OH})$
Optimal band (0.9–1.1 eV)			
ZrO ₂	mp-2574	(200)	0.9461
PbTiO ₃	mp-20459	(200)	0.9873
SrTiO ₃	mp-5229	(001)	1.0608
MgCo ₂ O ₄	mp-756442	(001)	0.9197
SrNiO ₃	mp-762506	(210)	0.9588
NiO	mp-1180047	(210)	0.9480
CaNiO ₃	mp-1368210	(210)	0.9958
ZnGa ₂ O ₄	mp-5794	(210)	1.0419

Continued on next page

Table 5 continued

Material	Identifier	Facet	$E_{\text{ads}}(*\text{OH})$
CaTi ₂ O ₆	mp-1079825	(210)	0.9755
RuO	oqmd-4372977	(210)	1.0445
LaNiO ₂	mp-20392	(001)	0.9456
BaFeO ₃	mp-19035	(111)	1.0901
CaNi ₂ O ₅	mp-1410425	(111)	0.9561
BaNiO ₃	mp-1120765	(111)	1.0578
BaNiO ₂	mp-18943	(001)	1.0464
SrMnO ₃	mp-19001	(001)	1.0436
La ₂ NiO ₄	mp-21326	(001)	1.0868
Pr ₂ NiO ₄	mp-18839	(001)	0.9131
Gd ₂ NiO ₄	mp-1207225	(001)	1.0750
Close band (0.8–1.2 eV)			
CaTiO ₃	mp-5827	(001)	0.8948
TiO ₂	mp-2657	(211)	0.8875
PbTiO ₃	mp-20459	(101)	1.1979
Co ₃ O ₄	mp-18748	(200)	0.8891
CoGa ₂ O ₄	mp-765466	(001)	1.1102
CoAl ₂ O ₄	mp-36447	(001)	1.1235
MnFe ₂ O ₄	mp-33708	(101)	0.8766
KNbO ₃	mp-7375	(101)	1.1770
SrNiO ₃	mp-762506	(001)	0.8111
LaCuO ₃	mp-3474	(101)	1.1084
CaNiO ₃	mp-1368210	(001)	1.1382
CaTi ₂ O ₆	mp-1079825	(101)	0.8324
FeNiO ₃	mp-1272388	(101)	0.6416

Continued on next page

Table 5 continued

Material	Identifier	Facet	$E_{\text{ads}}(*\text{OH})$
Nd ₂ NiO ₄	mp-19191	(001)	1.1307
SmNiO ₃	mp-1099668	(210)	0.8040
SmCoO ₃	mp-22549	(210)	1.1363
Sr ₂ NiO ₄	oqmd-5631134	(111)	0.8331
Near band (0.7–1.3 eV)			
NiFe ₂ O ₄	mp-22684	(001)	0.7186
NiFe ₂ O ₄	mp-22684	(200)	0.7111
LiFe ₂ O ₄	mp-25386	(001)	0.7298
CuFe ₂ O ₄	mp-770107	(001)	0.7448
ZnAl ₂ O ₄	mp-2908	(001)	1.2535
ZnAl ₂ O ₄	mp-2908	(210)	1.2963
ZnGa ₂ O ₄	mp-5794	(001)	1.2858
BiFeO ₃	mp-23501	(101)	0.7912
MgO	mp-1265	(210)	1.2428
SrNiO ₃	mp-762506	(111)	0.7144
Ga ₂ O ₃	mp-1243	(111)	0.7936
FeO	mp-756436	(001)	0.7784
CaNiO ₃	mp-1368210	(111)	0.7677
TiFe ₂ O ₄	mp-780585	(001)	0.7547
LaNiO ₃	mp-19339	(101)	1.2836
SrCoO ₃	mp-505766	(111)	0.7030
SrFeO ₃	mp-510624	(001)	0.7433
CaNiO ₂	mp-1147749	(001)	1.2370
CaNi ₂ O ₅	mp-1410425	(101)	1.2883
Sr ₂ MnO ₄	mp-18978	(101)	0.7463

Continued on next page

Table 5 continued

Material	Identifier	Facet	$E_{\text{ads}}(*\text{OH})$
Ba ₂ MnO ₄	mp-753330	(101)	0.7669
NdNiO ₃	mp-22106	(111)	0.6999
PrCoO ₃	mp-20427	(111)	0.7499
SmNiO ₃	mp-1099668	(001)	1.2208
SrRuO ₃	mp-22534	(001)	0.7271
Gd ₂ CoO ₄	oqmd-5233083	(111)	0.7364

ORR material selection rationale. The agent selected candidate oxides by combining domain knowledge of oxide electrocatalysis with automated structure retrieval. Below, the selection rationale and chemical interpretation of the *OH adsorption result are given for each unmodified Optimal-band material in Table 5.

ZrO₂ (mp-2574): Selected as a chemically robust, moderately reducible oxide; undercoordinated Zr–O motifs on (200) deliver near-volcano-optimal *OH binding (~ 1 eV). *PbTiO₃ (mp-20459)*: A titanate perovskite (ABO_3 tuning platform) where A-site chemistry and Ti–O covalency tune adsorbate binding; the (200) termination lands at the *OH optimum. *SrTiO₃ (mp-5229)*: Benchmark perovskite whose facets are heavily studied and readily strain/doping-tunable; (001) at ~ 1.06 eV indicates balanced *OH affinity consistent with perovskite trends. *MgCo₂O₄ (mp-756442)*: Co-based spinels are canonical ORR/OER oxide motifs; Mg on the A-site tunes Co oxidation/covalency, placing (001) in the optimal window. *SrNiO₃ (mp-762506)*: Ni perovskites are frequently ORR-active due to strong Ni–O covalency; the (210) facet gives near-ideal *OH binding. *NiO (mp-1180047)*: Simple, well-characterized reference oxide for Ni chemistry; (210) at ~ 0.95 eV provides a baseline single-oxide ORR descriptor match. *CaNiO₃ (mp-1368210)*: Extends the Ni-perovskite family by A-site contraction (Ca vs Sr/Ba/La), probing how lattice distortion tunes Ni–O bonding; (210) lands at ~ 1.0 eV. *ZnGa₂O₄ (mp-5794)*: Stable spinel used as an oxide benchmark;

(210) at ~ 1.04 eV is a non-transition-metal ($B=\text{Ga}$) comparator achieving near-ideal *OH binding via geometric effects. *CaTi₂O₆* (*mp-1079825*): Ti-rich Ca–Ti–O phase between CaTiO₃ and TiO₂, selected as an interpolation between known good titanates; (210) exposes a mixed Ti–O environment yielding near-ideal binding. *RuO* (*oqmd-4372977*): Situated between metallic Ru and RuO₂ in oxidation state; (210) of cubic RuO yields *OH adsorption near 1 eV, indicating balanced binding compared to more strongly binding RuO₂ facets. *LaNiO₂* (*mp-20392*): Infinite-layer nickelate related to LaNiO₃ with reduced oxygen content; (001) at ~ 0.95 eV sits squarely in the optimal window, suggesting balanced activity comparable to the best perovskite planes. *BaFeO₃* (*mp-19035*): Ba analogue of SrFeO₃/LaFeO₃, probing how A-site expansion tunes Fe⁴⁺–O covalency; (111) at ~ 1.09 eV is squarely in the optimal band. *BaNiO₃* (*mp-1120765*): Ba analogue of LaNiO₃/CaNiO₃, examining how expanding the A-site radius around Ni⁴⁺ affects surface adsorption; (111) at ~ 1.06 eV shows Ni–O covalency comparable to the best nickelate perovskites. *BaNiO₂* (*mp-18943*): More reduced, layered Ni oxide, the Ba-based counterpart to CaNiO₂/LaNiO₂; square-planar Ni on (001) delivers ~ 1.05 eV despite lower oxygen content. *SrMnO₃* (*mp-19001*): Extends Mn perovskite screening beyond LaMnO₃, targeting how a more ionic Sr²⁺ A-site influences *OH binding; (001) at ~ 1.04 eV shows Mn⁴⁺ perovskites can match the best Fe- and Ni-based systems. *La₂NiO₄* (*mp-21326*): The $n = 1$ Ruddlesden–Popper analogue of LaNiO₃, exposing layered NiO₂ planes separated by La–O rock-salt blocks; (001) binds *OH at ~ 1.09 eV, consistent with balanced Ni–O covalency. *Pr₂NiO₄* (*mp-18839*): Lighter rare-earth RP nickelate interpolating between La₂NiO₄ and Nd₂NiO₄; (001) at ~ 0.91 eV shows Pr-based RP layers slightly soften Ni–O binding while remaining catalytically balanced. *Gd₂NiO₄* (*mp-1207225*): Extends the RP nickelate series to a smaller, more strongly distorted lanthanide; (001) at ~ 1.08 eV indicates that even with significant structural distortion the K₂NiF₄ motif preserves near-ideal *OH binding.

The following Close- and Near-band materials from Tables 5 and 6 were not selected for iterative tuning but have documented screening reasoning: *FeNiO₃* (*mp-1272388*): Selected

as a mixed Fe–Ni oxide to probe synergy between NiO- and Fe₂O₃-like motifs; (101) at ~ 0.64 eV is on the weak-binding side. *Sr₂NiO₄ (oqmd-5631134)*: Alkaline-earth RP nickelate chosen as a charge-balanced, non-lanthanide reference to the La/Pr/Nd/Gd K₂NiF₄ nickelates; (111) at ~ 0.83 eV is slightly weaker than optimal.

ORR tuning history. The agent attempted strain and/or single-atom surface substitution on Close and Near band candidates to move their adsorption energies into the Optimal 0.9–1.1 eV window. Positive strain values denote in-plane compression (a, b scaled by $1-\epsilon$); negative values denote tensile strain. “Doping” refers to replacement of the topmost surface atom of the indicated element. Each run evaluated five Miller-index facets in parallel; only the best result per run is highlighted below. For each material, the *selection rationale* explains why it was chosen for tuning, and *rationale* entries document the strategic reasoning behind each attempted modification.

CaTiO₃ (mp-5827), Close (001) 0.8948 eV. *Selection:* CaTiO₃ is a canonical titanate perovskite ORR screening reference; starting slightly weak on *OH makes it ideal for small, physically plausible strain/dopant nudges into the target optimum. Run A (Ti→Zr doping, -2% tensile): (001) 1.14, (100) 1.14 eV—too strong. *Rationale:* isovalent Zr substitution plus tensile strain to perturb Ti–O reactivity and strengthen *OH on borderline facets; it overshot on (001)/(100) and destabilized other terminations. Run B (-1% tensile, no doping): (001) 0.9907 eV (**optimal**), (100) 0.9930 eV (**optimal**). *Rationale:* mild tensile strain as the minimal-change knob to strengthen *OH slightly without changing chemistry; successfully moved (001)/(100) into the optimal band.

TiO₂ (mp-2657), Close (211) 0.8875 eV. *Selection:* TiO₂ is a foundational oxide for ORR benchmarking and facet chemistry; the well-studied rutile (211) being slightly weak on *OH makes it a targeted candidate for gentle tuning. Run A (Ti→Zr doping, $+1\%$ compressive): all facets overbinding (-3.46 to -0.06 eV). *Rationale:* tested Zr substitution

plus compressive strain as a first-pass electronic/structural perturbation; it drove many terminations into severe overbinding. Run B (−1% tensile, no doping): (211) 1.0475 eV (**optimal**), (101) 0.9400 eV (**optimal**). *Rationale*: removed dopant disorder and used mild tensile strain alone to shift adsorption toward balanced binding on the target facet.

CoAl₂O₄ (mp-36447), Close (001) 1.1235 eV. *Selection*: CoAl₂O₄ is a stable spinel proxy for Co-centered ORR motifs; starting slightly strong on *OH makes it a good test of whether small elastic strain can soften binding into the volcano optimum. Run A (+2% compressive): (001) 1.0948 eV (**optimal**), (100) 1.0919 eV (**optimal**). *Rationale*: used strain as a gentle, chemistry-preserving knob to soften slightly-overbinding (001)/(100) terminations; +2% compressive was sufficient.

CoGa₂O₄ (mp-765466), Close (001) 1.1102 eV. *Selection*: CoGa₂O₄ is a Co-spinel analogue where swapping Al↔Ga and applying strain can tune Co–O covalency; (001) just above the *OH optimum makes it a prime nudge candidate. Run A (Ga→Al doping, +2%): (001) 1.22 eV—too strong. *Rationale*: tried Al substitution plus compressive strain to adjust surface ionicity/covalency; it pushed (001) farther from optimal. Run B (+2% compressive): (001) 1.20 eV—still high. *Rationale*: isolated the strain effect (removing dopant) to see if compression alone would soften binding; still too strong. Run C (−2% tensile): (001) 1.0584 eV (**optimal**). *Rationale*: switched strain sign to tensile after compression failed; correctly softened the slightly-overbinding (001) into the optimal band.

KNbO₃ (mp-7375), Close (101) 1.177 eV. *Selection*: KNbO₃ is a Nb-based ABO₃ perovskite (different B-site chemistry than Ti/Fe/Ni) used to diversify the ORR oxide space; strong facet dependence makes it a good target for finding a termination with near-ideal binding. Run A (+3% compressive): (111) 0.9273 eV (**optimal**). *Rationale*: focused on the (111) termination to change Nb–O coordination and used moderate compressive strain to soften overly strong binding from other facets; (111) landed in the optimal band.

Nd₂NiO₄ (mp-19191), Close (001) 1.1307 eV. *Selection:* Nd₂NiO₄ is the Nd member of the RP nickelate family between Pr₂NiO₄ and Gd₂NiO₄, tracking how lanthanide contraction tunes surface reactivity. Run A (+2% compressive): (001) 1.14 eV—still high. *Rationale:* tested small compressive strain as a conservative first knob; it shifted the wrong direction. Run B (−2% tensile): (001) 2.30 eV—too weak. *Rationale:* explored opposite strain sign; it over-softened *OH on (001). Run C (no modifications): (001) 1.13 eV—still high. *Rationale:* re-ran baseline to confirm starting regime before adding chemical perturbations. Run D (Ni→Co doping): (001) 0.86 eV—too weak. *Rationale:* introduced Co at surface to weaken Ni-centered adsorption by changing d-electron filling; it overshot into weak binding. Run E (Ni→Co doping, −1% tensile): (001) 1.0880 eV (**optimal**). *Rationale:* combined Co substitution (major tuning) with mild strain (fine tuning) to restore balanced binding.

SmNiO₃ (mp-1099668), Close (210) 0.8040 eV. *Selection:* SmNiO₃ is a more distorted rare-earth nickelate perovskite, continuing the Nd/Pr series to probe the effect of increasing octahedral tilts; (210) at 0.80 eV indicates that Sm-induced distortions noticeably reduce adsorption strength. Run A (−1% tensile): (210) 0.897 eV—just below optimal. *Rationale:* applied mild tensile strain to strengthen *OH on the weak-binding (210) facet; nearly reached the target window. Run B (−1.5% tensile): (210) 0.70 eV—overshot. *Rationale:* swept strain magnitude to gauge sensitivity; it weakened binding too far. Run C (Ni→Cu doping, −1%): (210) 0.82 eV—still weak. *Rationale:* tested Cu substitution to alter surface electronic structure and strengthen adsorption; insufficient. Run D (−1.1% tensile): (210) 0.9066 eV (**optimal**). *Rationale:* fine-tuned strain between the “almost” and “overshot” cases to land precisely in the target window.

SmCoO₃ (mp-22549), Close (210) 1.1363 eV. *Selection:* SmCoO₃ is a Co-based analogue of LaCoO₃ and PrCoO₃, exploring Co³⁺/O covalency in a smaller A-site environment; (210) at ~1.14 eV is slightly strong. Run A (+2% compressive): all facets overbinding.

Rationale: tried compressive strain first as a chemistry-preserving knob; other terminations remained excessively reactive. Run B (+0.5% compressive): (210) 1.13 eV—still high. *Rationale:* reduced strain magnitude for a finer adjustment; (210) stayed just outside the window. Run C (Co→Fe doping): (210) 1.0681 eV (**optimal**). *Rationale:* used Fe substitution to moderate Co–O covalency and soften adsorption on the reactive surface site.

Co₃O₄ (mp-18748), Close (200) 0.8891 eV. *Selection:* Co₃O₄ is a prototypical Co-spinel frequently discussed for ORR/OER; its *OH binding just below the target made it a logical tune-up candidate. Run A (Co→Zn doping, −1%): (200) 0.88 eV. *Rationale:* introduced Zn to tune Co-site reactivity and used mild tensile strain to strengthen borderline *OH; insufficient. Run B (−5% tensile): (200) 0.85 eV. **No success.** *Rationale:* tried larger strain-only adjustment; still could not lift (200) into optimal.

LaCuO₃ (mp-3474), Close (101) 1.1084 eV. *Selection:* LaCuO₃ was included as a Cu-perovskite out-of-family comparator to test late transition-metal oxides; near-optimal baseline but tuning destabilized facets. Run A (+1% compressive): (101) 1.46 eV—too strong. **No success.** *Rationale:* applied small compressive strain to soften slightly-strong *OH; instead it increased binding strength.

MnFe₂O₄ (mp-33708), Close (101) 0.8766 eV. *Selection:* MnFe₂O₄ is a mixed Mn/Fe spinel chosen to probe bimetallic-site synergy; near-target *OH suggested tunability but strain drove the system away. Run A (−3% tensile): all facets too weak or overbinding. **No success.** *Rationale:* used tensile strain to strengthen borderline *OH on (101) without changing composition; it substantially weakened adsorption across facets.

CaTi₂O₆ (mp-1079825), Close (101) 0.8324 eV. *Selection:* Close-band (101) facet was targeted for tuning; the (210) facet already achieved optimal in the pristine screen (Table 5). Run A (−2% tensile): AdsorbML error—identifier not found. **Not runnable** in

this environment.

CaNi₂O₅ (mp-1410425), Near (101) 1.2883 eV. *Selection:* CaNi₂O₅ is a mixed-valence Ni oxide interpolating between NiO- and CaNiO₃-like chemistries, inspired by the strong performance of LaNiO₃ and SrNiO₃; strong-binding (101) at the Near edge suggested potential for softening. Run A (Ni→Co doping): (111) 1.0070 eV (**optimal**), (100) 0.90 eV. *Rationale:* substituted Co on the surface B-site to weaken overly strong Ni-centered adsorption; the dense (111) facet landed squarely in the optimal region.

PrCoO₃ (mp-20427), Near (111) 0.7499 eV. *Selection:* PrCoO₃ is the Pr-based Co perovskite analogue to LaCoO₃, probing how replacing La with a smaller rare earth alters Co–O covalency; (111) shows relatively weak *OH binding. Run A (–5% tensile): (111) 0.74 eV—still weak. *Rationale:* used large tensile strain to strengthen *OH without changing composition; minimal effect. Run B (Co→Cu doping): (111) 0.87 eV—still below optimal. *Rationale:* tested Cu substitution to tune surface electronic structure toward stronger adsorption; moved closer but remained sub-optimal. Run C (Co→Zn doping): (111) 0.9606 eV (**optimal**). *Rationale:* used Zn substitution to perturb surface-site reactivity and strengthen adsorption without triggering overbinding.

CaNiO₂ (mp-1147749), Near (001) 1.2370 eV. *Selection:* CaNiO₂ is a reduced, infinite-layer-like Ni phase chosen to test how oxygen deficiency shifts *OH adsorption relative to perovskite nickelates; strong-binding (001) suggested potential for softening. Run A (Ni→Co): (001) 1.22 eV. *Rationale:* introduced Co to weaken overly strong Ni-centered adsorption; reduced binding only slightly. Run B (Ni→Co, +2%): (001) 1.18 eV. *Rationale:* combined Co substitution with compressive strain to amplify the weakening; still insufficient. Run C (Ni→Fe): (001) 0.44 eV. **No success.** *Rationale:* tried Fe substitution as a stronger perturbation; it over-softened into unphysically weak binding.

Sr₂MnO₄ (mp-18978), Near (101) 0.7463 eV. *Selection:* Sr₂MnO₄ is an RP Mn oxide chosen to test whether layering (vs 3D perovskites) shifts Mn–O reactivity; began weak on *OH. Run A (+3% compressive): best facet (111) 0.82 eV. *Rationale:* applied compressive strain to strengthen weak *OH while keeping composition fixed; increased adsorption only modestly. Run B (Mn→Ti doping, +3%): (001) 0.70 eV. **No success.** *Rationale:* introduced Ti to tune Mn-centered surface reactivity under strain; it further weakened adsorption.

SrRuO₃ (mp-22534), Near (001) 0.7271 eV. *Selection:* SrRuO₃ is a Ru-perovskite analogue included because Ru oxides are high-activity oxygen electrocatalysts; weak-binding (001) tested whether strain could push Ru–O surfaces toward the *OH optimum. Run A (–5% tensile): (001) 0.88 eV—still below optimal. **No success.** *Rationale:* used large tensile strain to strengthen adsorption on a weak-binding facet; improved but still fell short.

FeO (mp-756436), Near (001) 0.7784 eV. *Selection:* FeO is a simple Fe²⁺ oxide reference for isolating single-site Fe–O chemistry; screened to compare against Fe-perovskites/spinels. Run A (–5% tensile): facets either too weak or overbinding. **No success.** *Rationale:* applied large tensile strain to strengthen weak-binding facets; the response was non-uniform across terminations and no facet reached optimal.

ZnAl₂O₄ (mp-2908), Near (001) 1.2535 eV. *Selection:* ZnAl₂O₄ is a stable, non-redox spinel used as a structural/ionicity comparator; strong *OH binding tested whether purely elastic tuning can soften adsorption in a chemically inert spinel. Run A (+5% compressive): (001) 1.55 eV—worse. **No success.** *Rationale:* used aggressive compressive strain; it pushed binding further from optimal and triggered slab-generation issues.

Away-band facets. Table 6 lists all material–facet combinations whose $E_{\text{ads}}(*\text{OH})$ fell outside the 0.7–1.3 eV Near band. These represent facets with either strong overbinding (large negative energies) or very weak adsorption (large positive energies).

Table 6: Raw agent *OH adsorption energies—Away band (outside 0.7–1.3 eV). Multiple facets per material are listed together. Energies in eV.

Material	Identifier	Facets and energies [eV]
CaTiO ₃	mp-5827	(111) -2.28, (101) -2.43, (210) 0.68
RuO ₂	mp-825	(111) -5.15, (210) 0.07, (200) -5.01, (211) 0.61
TiO ₂	mp-2657	(111) 0.62, (200) -6.47
ZrO ₂	mp-2574	(001) -7.88, (101) -4.60, (210) -0.74
PbTiO ₃	mp-20459	(111) -0.24, (210) 0.48
SrTiO ₃	mp-5229	(101) -2.36, (210) 0.34
BiVO ₄	mp-545850	(111) -0.82, (210) -1.96, (211) 0.57
Co ₃ O ₄	mp-18748	(101) -0.12, (210) 0.63, (211) -0.68
CoGa ₂ O ₄	mp-765466	(111) -5.55, (101) -0.87, (210) 0.33
MgCo ₂ O ₄	mp-756442	(101) -0.81, (210) 0.03
CoAl ₂ O ₄	mp-36447	(111) -4.67, (101) -1.38, (210) -0.22
SnO ₂	mp-856	(111) 0.59, (101) 0.62, (210) 0.35, (200) 0.20
IrO ₂	mp-2723	(111) -0.54, (001) -0.17, (210) -4.30, (200) -4.50
NiFe ₂ O ₄	mp-22684	(101) -0.38, (210) 0.34
MnO ₂	mp-510408	(111) -0.21, (101) 0.66, (210) 0.09, (200) 0.12
LiFe ₂ O ₄	mp-25386	(111) -1.09, (101) -0.01, (210) 0.60
CuFe ₂ O ₄	mp-770107	(111) -2.90, (101) -0.31, (210) 0.31
ZnAl ₂ O ₄	mp-2908	(101) -2.24
ZnGa ₂ O ₄	mp-5794	(111) -1.15, (101) -0.49
CoFe ₂ O ₄	mp-753222	(001) 0.57, (101) -0.48, (210) 0.37, (200) 0.57
LaCoO ₃	mp-510611	(111) 0.59, (210) 0.23
Ca ₂ Fe ₂ O ₅	mp-1096887	(001) -1.27, (101) -0.34, (210) -0.16, (200) -0.95
LaCrO ₃	mp-19357	(111) -1.81, (001) -1.40, (101) -0.73, (210) -1.85
CoCr ₂ O ₄	mp-20758	(001) -0.04, (101) -0.66, (210) 0.13, (200) -0.13
CoMn ₂ O ₄	mp-1222025	(001) 0.38, (101) -0.42, (210) -0.05
MnFe ₂ O ₄	mp-33708	(001) 0.14, (210) 0.08, (200) -0.59
CaFe ₂ O ₄	mp-1405146	(111) -4.01, (001) 0.69, (101) -1.17, (210) -0.17
BiFeO ₃	mp-23501	(001) 0.43, (210) 0.13, (200) -0.05
ZnFe ₂ O ₄	mp-19313	(001) 0.62, (101) -0.54, (210) 0.35, (200) 0.62
Fe ₂ O ₃	mp-19770	(101) -0.08, (210) 0.20, (200) 0.47, (211) 0.38
LaMnO ₃	mp-19168	(111) -1.07, (001) -0.80, (101) -0.06, (210) -0.88
Cu ₂ O	mp-361	(101) 1.34, (210) 0.08, (200) -0.58, (211) -0.96
LaFeO ₃	mp-22590	(111) -0.89, (001) -0.15, (101) -1.01, (210) -1.52
BeO	mp-2542	(111) -5.75, (001) -3.72, (101) -3.52, (210) -4.25
KNbO ₃	mp-7375	(001) -1.96, (200) -2.52
WO ₃	mp-19390	(111) -3.70, (101) -2.23, (210) 0.19, (200) -0.02

Continued on next page

Table 6 continued

Material	Identifier	Facets and energies [eV]
CeO ₂	mp-20194	(101) -0.24, (210) -3.70
Sr ₂ FeO ₄	mp-19102	(101) 0.61, (210) -0.62
YNiO ₃	mp-19242	(111) -0.01, (001) -1.38, (210) -1.41
CoO	mp-19128	(001) -3.19, (101) 0.37, (210) 0.10, (200) 0.19
MgO	mp-1265	(001) 2.34, (101) 0.61, (200) 2.34
ZnO	mp-2133	(001) -1.24, (101) -1.17, (210) 1.80, (200) 1.40
MnO	mp-19006	(210) -0.33, (200) -0.68
CuO	mp-1692	(001) -0.83, (101) -0.88, (210) -3.08, (200) 2.08
ZnCr ₂ O ₄	mp-19410	(111) -1.87, (001) -0.77, (101) -0.83, (210) -0.46
MgFe ₂ O ₄	mp-608016	(001) 0.64, (101) -1.00, (210) -0.04, (200) 0.66
In ₂ O ₃	mp-22598	(001) -0.88, (101) -0.06, (210) -0.54, (200) -0.88
SrNiO ₃	mp-762506	(101) -0.30
NiO	mp-1180047	(101) 1.92
Ga ₂ O ₃	mp-1243	(101) -1.25, (210) -1.28, (200) -1.16
FeO	mp-756436	(210) -0.87, (200) 0.27
LaCuO ₃	mp-3474	(111) 0.07, (001) -0.14, (210) -0.51
CaNiO ₃	mp-1368210	(101) 0.60
TiFe ₂ O ₄	mp-780585	(111) -0.35, (101) -1.20, (210) -1.11
CdFe ₂ O ₄	mp-21333	(001) 0.30, (101) -0.44, (210) 0.23, (200) 0.29
LaNiO ₃	mp-19339	(111) -0.07, (001) -0.42, (210) -0.64
Ca ₂ TiO ₄	mp-1096860	(110) -2.88
CaTiO ₂	mp-1385378	(001) -3.25

S3.2 NRR: *N and *N₂ Adsorption Energies

The agent screened binary intermetallic alloys for the nitrogen reduction reaction using two descriptors: $E_{\text{ads}}(*\text{N})$ within $[-2.0, -0.5]$ eV and $\Delta = E_{\text{ads}}(*\text{N}) - E_{\text{ads}}(*\text{N}_2) > 0$ eV. Materials were classified as *Good* ($\Delta > 0$ with E_{N} in-window), *Near-miss* ($-0.2 < \Delta < 0$), or *Not meeting criteria*. Table 7 lists the good surfaces. Tables 8 and 9 list near-miss and iteratively optimized surfaces.

Table 7: Raw agent NRR screening—Good surfaces ($\Delta > 0$ eV, $E_N \in [-2.0, -0.5]$ eV). Energies in eV.

Material	Identifier	Facet	E_N	E_{N_2}	Δ	Modification
PtFe	mp-2260	(100)	-0.76	-0.79	+0.03	Pristine
PtFe	mp-2260	(111)	-0.79	-0.87	+0.08	+3% strain
CoNi	mp-1006883	(111)	-0.54	-0.65	+0.11	Pristine
CoNi	mp-1006883	(211)	-0.61	-0.66	+0.06	Pristine
RhCo	mp-1226026	(100)	-0.63	-0.77	+0.14	Pristine
IrMo	mp-1221414	(211)	-0.64	-0.76	+0.12	Pristine
HfPd	mp-1002106	(211)	-1.84	-2.24	+0.40	Pristine
FeNi	mp-2213	(100)	-0.92	-1.05	+0.13	Pristine
Ni ₄ Mo	mp-11507	(111)	-0.61	-0.63	+0.02	Mo→Ni doping
IrRe	mp-1219533	(110)	-0.56	-0.70	+0.15	Pristine
CuFe	mp-1224945	(110)	-0.79	-3.06	+2.27	+12% strain [†]

[†]Extreme strain; treat with caution due to many anomalous configurations.

NRR good-surface selection and screening rationale. For each material in Table 7, the selection rationale explains why the alloy was screened, and the run rationale documents the reasoning behind each trial.

CoNi (mp-1006883): Co–Ni alloys are inexpensive, conductive, and offer tunable N-binding via alloy/ensemble effects while staying away from extreme early-TM overbinding. Both facets bind *N near the weak end of the target window with positive Δ , favoring desorption and NRR selectivity. *Run 0 (pristine)*: baseline multi-facet check confirmed E_N in-window and $\Delta > 0$.

RhCo (mp-1226026): Adding a noble-metal component (Rh) to Co softens overly reactive Co-like sites while preserving activation at undercoordinated ensembles. The (100) facet shows moderate positive Δ . *Run 0 (pristine)*: single-shot evaluation because the pristine

surface already satisfies thresholds.

IrMo (mp-1221414): Mo is a classic N-activating element while Ir can moderate binding/poisoning; the alloy targets balanced activation without the extreme overbinding of pure early TMs. *Run 0 (pristine)*: direct test of a step facet (211) where N₂ activation is most likely.

HfPd (mp-1002106): Early TM–Pd intermetallic to access stronger N activation motifs (Hf) tempered by a late TM (Pd) to avoid complete poisoning. The (211) step binds *N on the strong side of the window. *Run 0 (pristine)*: step-site probe to see whether an early-TM ensemble can meet Δ and still remain within the E_N window.

PtFe (mp-2260): Fe–Pt is a canonical “reactive (Fe) + moderating (Pt)” bimetal where small tuning can move near-miss energetics across the Δ threshold. *N is well within the optimal window and only marginally more stable than *N₂, close to the Δ cutoff. *Run 0 (pristine recompute)*: verified the near-miss $\Delta \approx -0.02$ eV before tuning. *Run 1 (+3% compressive)*: adjusted surface electronic structure to shift relative *N/*N₂ stability and flip Δ positive while keeping E_N in-window.

FeNi (mp-2213): Fe–Ni (tetrataenite-like) is a cheap, widely studied alloy where dual-site/ensemble effects can tune N activation. *Run 0 (pristine recompute)*: re-optimized adsorption minima; found a lower-energy *N₂ configuration that flipped Δ positive.

Ni₄Mo (mp-11507): Classic Ni–Mo electrocatalyst platform; Mo provides N-activation tendency while Ni moderates binding and offers scalable metallic conductivity. *Run 0 (pristine recompute)*: confirmed near-miss $\Delta < 0$. *Run 1 (+3% compressive)*: tested whether strain can improve Δ (it worsened). *Run 2 (−3% tensile)*: tested opposite direction (no improvement). *Run 3 (Mo→Ni top-layer)*: changed the local adsorption ensemble to weaken over-stabilization of *N and nudge Δ across zero—successful.

IrRe (mp-1219533): Re–Ir alloys are screened as “late TM + refractory TM” mixes that can stabilize activated N at steps without falling into early-TM overbinding extremes. *Run 0 (pristine recompute)*: verified Δ robustness by re-finding the lowest-energy *N₂ minimum;

Δ flipped positive on (110).

CuFe (mp-1224945): Cu–Fe is screened as a “weak-binding diluent (Cu) + activating center (Fe)” alloy. $\Delta > 0$ was achieved only at +12% compressive strain, which produced many anomalous configurations; treated with caution.

Table 8: Raw agent NRR screening—Near-miss surfaces ($-0.2 < \Delta < 0$ eV) with optimization attempts. Energies in eV.

Material	ID	Facet	E_N	E_{N_2}	Δ	Optimization outcome
Pd ₃ Mo	mp-1221429	(211)	-0.86	-0.71	-0.14	5 trials (strain, doping); Δ remained < 0
PdFe	mp-2831	(100)	-1.05	-0.99	-0.06	5 trials; best $\Delta = -0.016$ on (100) -3% tensile
CoRu	mp-1225997	(111)	-0.67	-0.61	-0.06	4 trials; best $\Delta = -0.043$ (Co→Ru doping)
Ni ₂ Mo	mp-784630	(111)	-0.71	-0.60	-0.11	Mo→Ni doping: $\Delta = -0.11$; no success
RuFe	mp-1224803	(111)	-0.71	-0.59	-0.12	Fe→Ru doping: $\Delta = -0.11$; no success
RuPt	mp-1120769	(100)	-0.80	-0.69	-0.11	+3% strain: $\Delta = -0.091$; no success
FeMo	oqmd-4484232	(111)	-0.99	-0.99	-0.01	Re-run: $E_N = -3.25$ (overbinding); reclassified
ZrPt	mp-11554	(211)	-1.31	-1.30	-0.01	Re-run: $\Delta = -0.29$ on (211); reclassified

NRR near-miss selection and optimization rationale. *Pd₃Mo (mp-1221429)*: Pd–Mo intermetallic combining a late TM (Pd) with an N-activating element (Mo); 5 trials including $\pm 3\%$ strain and Mo \leftrightarrow Pd substitutions all worsened or failed to recover $\Delta > 0$. *PdFe (mp-2831)*: Fe–Pd “activation + moderation” alloy; best result was $\Delta = -0.016$ on (100)

with -3% tensile—close but still negative. Compressive strain pushed E_N out of window. *CoRu* (*mp-1225997*): Co–Ru alloy where Ru shifts Co reactivity; 4 trials including strain and Co→Ru doping; Co→Ru gave the closest result ($\Delta = -0.043$) but still failed. *Ni₂Mo* (*mp-784630*): Ni–Mo motif variant testing Mo fraction/site density vs Ni₄Mo; Mo→Ni substitution slightly improved Δ (-0.11) but remained negative. *RuFe* (*mp-1224803*): Fe–Ru comparing how Ru replaces Pd/Pt; Fe→Ru doping improved Δ from -0.14 to -0.11 but did not cross zero. *RuPt* (*mp-1120769*): Ru–Pt “active + noble” blend; $+3\%$ strain improved Δ from -0.11 to -0.09 but was insufficient. *FeMo* (*oqmd-4484232*): Fe–Mo probing the strong-activation region; recomputed pristine showed $E_N = -3.25$ eV (overbinding), so the initial near-ideal result was an artifact of not finding the global minimum. Reclassified as not meeting criteria. *ZrPt* (*mp-11554*): Zr–Pt early-TM + noble intermetallic; recomputed (211) gave $\Delta = -0.29$, ruling out the earlier near-isoenergetic result. Reclassified as not meeting criteria.

Table 9: Raw agent NRR screening—Iteratively optimized candidates (originally non-viable pristine surfaces rescued by doping/strain). Energies in eV.

Material	ID	Modification	Facet	E_N	E_{N_2}	Δ
CoPt	mp-1225998	Pt→Fe, $+3\%$ strain	(100)	-0.64	-0.73	$+0.10$
CoPt	mp-1225998	Pt→Fe, $+3\%$ strain	(110)	-0.68	-0.94	$+0.26$
CoPt	mp-1225998	Pt→Fe, $+3\%$ strain	(211)	-0.62	-0.92	$+0.30$
PdRu	mp-1186459	Pd→Fe, no strain	(100)	-0.62	-0.84	$+0.22$
PdRu	mp-1186459	Pd→Fe, $+3\%$ strain	(211)	-0.54	-0.57	$+0.03$
TiPt ₃	mp-12107	Pt→Fe, no strain	(110)	-0.50	-0.85	$+0.35$
TiPt ₃	mp-12107	Pt→Fe, no strain	(311)	-1.15	-1.35	$+0.20$
PtRh	mp-1219734	Pt→Fe, no strain	(100)	-0.55	-0.60	$+0.05$
PtRh	mp-1219734	Pt→Fe, no strain	(311)	-0.54	-0.64	$+0.10$

NRR iterative optimization rationale. The following materials had no viable pristine facet but were rescued by surface-site engineering (single-atom substitution \pm strain).

CoPt (mp-1225998): Co–Pt is a stable late-TM alloy too weak-binding for NRR in pristine form (E_N positive or < -0.5 eV on all facets), making it a test of “surface-site engineering.” *Run 0 (pristine)*: confirmed weak E_N across (111)/(100)/(110)/(211)/(311). *Run 1 (+3% strain)*: strain alone did not move E_N into the target window. *Run 2 (–3% tensile)*: opposite strain also failed. *Run 3 (Pt \rightarrow Fe, no strain)*: introduced a stronger-binding surface site; (211) became viable ($\Delta \approx +0.16$). *Run 4 (Pt \rightarrow Fe, +3% strain)*: combined electronic/strain tuning to satisfy both E_N and Δ on (100), (110), and (211).

PdRu (mp-1186459): Pd–Ru is a late-TM platform typically too weak for N activation. *Run 0 (pristine)*: confirmed weak/positive E_N adsorption. *Run 1 (Pd \rightarrow Fe, no strain)*: created a stronger-binding ensemble; (100) became viable ($\Delta \approx +0.22$). *Run 2 (Pd \rightarrow Fe, +3% strain)*: fine-tuned adsorption balance on the doped surface; (211) also became viable.

TiPt₃ (mp-12107): Pt₃Ti intermetallic with distinct Pt-rich site types where Δ issues can be corrected by localized site strengthening. *Run 0 (pristine)*: (110) had E_N in window but $\Delta \approx -0.29$ (too negative). *Run 1 ($\pm 3\%$ strain)*: did not fix Δ on (110) and worsened it on other facets. *Run 2 (Pt \rightarrow Fe, no strain)*: Fe substitution corrected the overly strong preference for atomic E_N , producing balanced E_N vs E_{N_2} on (110) and (311).

PtRh (mp-1219734): Pt–Rh is an archetypal noble alloy expected to be too weak for E_N —included as a “can site engineering rescue weak binders?” benchmark. *Run 0 (pristine)*: confirmed weak-binding baseline (E_N positive on all facets). *Run 1 (Pt \rightarrow Fe, no strain)*: a single Fe surface atom supplied the necessary binding strength while preserving a small positive Δ on (100) and (311).

Materials not meeting NRR criteria. The following materials had no surface among the tested facets that simultaneously satisfied both $E_N \in [-2.0, -0.5]$ eV and $\Delta > -0.2$ eV in their pristine form. Each was selected based on its expected electronic/chemical properties,

and the dominant failure mode is indicated in parentheses. Pt-based: Pt₃Co (E_N too weak), CrPt (E_N out of window), OsPt₃ (E_N too weak), HfPt ($\Delta \ll -0.2$), Ta₃Pt (E_N too strong or $\Delta \ll -0.2$), MnPt (E_N too weak). Pd-based: PdRe ($\Delta \ll -0.2$), PdNi (E_N too weak), CuPd (E_N positive), Cu₃Pd₂ (E_N positive), CuPd₃ (E_N positive), ZrPd ($E_N < -2.0$ or $\Delta \ll -0.2$). Cu-based: CuZn (E_N strongly positive), Cu₃Zn (E_N strongly positive), CuZn₃ (E_N strongly positive), CuNi (E_N too weak), CoCu (E_N too weak or < -2.0), AuCu (E_N strongly positive), CuMo ($\Delta \ll -0.2$). Fe–Co: Fe₂Co ($\Delta \ll -0.2$), FeCo ($\Delta \leq -0.2$ on viable facets), FeW ($\Delta \ll -0.2$). Ni-based: WNi (no facet satisfies both constraints). Ru-based: RuAu ($\Delta \leq -0.2$ or missing *N₂ data). Ir-based: GaIr (E_N positive). Au-based: AuPt ($E_N > 0.7$ eV), AuPd ($E_N > 1.2$ eV). Mo/V/Nb-based: MoW ($E_N < -2.0$ and $\Delta \ll -0.2$), MoV ($E_N < -2.0$ or $\Delta \ll -0.2$), VW ($\Delta \ll -0.2$), VCr ($\Delta \ll -0.2$).

S3.3 CO₂ Reduction Reaction: *CO and *H Adsorption Energies

The agent screened intermetallic and elemental surfaces for CO₂ reduction to CO using two concurrent descriptors: $E_{\text{ads}}(*\text{CO}) \in [-0.82, -0.52]$ eV and $E_{\text{ads}}(*\text{H}) \geq +0.33$ eV. All structures were provided as local CIF files from the Catalysis Hub database. Table 10 lists all 13 materials screened and their base (unmodified) adsorption energies.

Table 10: Raw agent CO₂RR screening—base (unmodified) adsorption energies. Energies in eV.

Material	CIF	Facet	$E(*\text{CO})$	$E(*\text{H})$	Base status
Pb ₃ Y	Pb3Y.cif	(111)	-0.738	+0.379	PASS
Sn ₃ Y	Sn3Y.cif	(111)	-0.620	+0.513	PASS
Sn ₃ Sc	ScSn3.cif	(111)	-0.730	+0.465	PASS
Tl ₃ La	LaTl3.cif	(111)	-0.613	+0.237	FAIL (H low)
In ₃ Y	In3Y.cif	(111)	-0.799	+0.170	FAIL (H low)
Au ₃ Sc	Au3Sc.cif	(111)	-0.615	+0.094	FAIL (H low)
Au ₃ Y	Au3Y.cif	(111)	-0.647	-0.220	FAIL (H low)

Table 10 continued

Material	CIF	Facet	$E(*CO)$	$E(*H)$	Base status
In ₃ La	In3La.cif	(111)	-0.591	+0.119	FAIL (H low)
Al ₃ Rh	Al3Rh.cif	(111)	-0.580	+0.291	FAIL (H low)
Al ₃ Ni	Al3Ni.cif	(111)	-0.433	+0.351	FAIL (CO weak)
Cd ₃ Pt	Cd3Pt.cif	(111)	-0.894	-0.132	FAIL (both)
Cu	Cu.cif	(511)	-0.638	-0.044	FAIL (H low)
YN	YN.cif	(110)	-0.401	-0.241	FAIL (both)

CO₂RR material selection rationale. All structures were sourced as local CIF files from the Catalysis Hub database. Below, the selection rationale for each material in Table 10 is given.

Pb₃Y: $L1_2 A_3B$ intermetallic with a p-block A-site (Pb) screened to weaken H binding while retaining moderate *CO binding; Y tunes electron donation and CO affinity. Pristine (111) simultaneously meets both targets. *Sn₃Y*: Sn-based intermetallics are CO₂RR-relevant p-block platforms; alloying with an electropositive element (Y) tunes *CO binding while keeping *H weak to suppress HER. Pristine (111) hits both targets without tuning. *Sn₃Sc*: Chosen as a Sn₃Y analogue to test how swapping the B-site (Y→Sc) shifts *CO/*H via electronegativity/size while staying in the same A_3B structural family. Retains in-window *CO and weak *H. *Tl₃La*: Heavy p-block surfaces often suppress H adsorption while keeping *CO in a workable range; La provides a strong electronic lever for tuning. Pristine had ideal *CO but *H slightly too favorable; small compressive strain rescued *H. *In₃Y*: In chemistry is CO₂RR-relevant and provides moderate CO binding; near-ideal *CO at pristine made it a high-leverage strain candidate. Rescued at +8.5% strain. *Au₃Sc*: Au-containing intermetallics preserve good conductivity and often land *CO in-range; all tuning targeted pushing *H above +0.33 eV without shifting *CO out of window. Not rescued. *Au₃Y*: Companion to Au₃Sc with a different rare-earth partner to test whether changing the B-site

could preserve Au-like *CO while weakening H binding. Strain improved *H but broke *CO. *In₃La*: In-based *A₃B* intermetallic with La B-site; *CO was in-range but *H remained too favorable despite strain and La→Y doping. *Al₃Rh*: Near-miss case (*H = +0.291 eV, just below threshold) where small strain or late-metal substitution might suffice; *H was not strain-rescuable without breaking *CO. *Al₃Ni*: Inverse-failure case where *H already met the threshold but *CO was too weak (−0.433 eV); tensile strain brought *CO in-range but collapsed *H. *Cd₃Pt*: Late-TM intermetallic testing whether Pt-based ensembles could be tuned into in-window *CO while suppressing *H. Both descriptors failed at base; *H stayed negative even when *CO was rescued. *Cu*: Canonical CO₂RR reference surface (Cu(511) step); acceptable *CO but *H far too favorable (HER-prone). Tuning could not suppress H adsorption. *YN*: Nitride included as a chemically distinct class to test whether polar/covalent anion frameworks shift *CO/*H away from metal-alloy trends. Both descriptors failed; doping worsened *H.

CO₂RR optimization history. The agent performed multiple optimization rounds (strain and surface doping) on the 10 materials that failed the base screening. For each material, the *rationale* entries document the strategic reasoning behind each attempted modification.

Tl₃La (111). *Run 0 (no modifications):* $E(*CO) = -0.613$ eV (in-range), $E(*H) = +0.237$ eV (too low). *Rationale:* baseline confirmed *CO correct and isolated *H as the only failure mode. +5% compressive strain: $E(*CO) = -0.619$ eV (in-range), $E(*H) = +0.332$ eV ($\geq +0.33$) → **PASS**. *Rationale:* applied strain to shift surface electronic structure and weaken *H while preserving in-window *CO.

In₃Y (111). *Rationale:* *CO was near-ideal at baseline (−0.799 eV); *H increased monotonically with compressive strain while *CO stayed in-window, motivating a strain sweep. +5%: $E(*H) = +0.258$ (low). +8%: $E(*H) = +0.322$ (low). +8.5%: $E(*CO) = -0.773$ eV, $E(*H) = +0.334$ eV → **PASS**. Fine-tuned strain in a narrow band to cross the *H cutoff.

Au₃Sc (111). *Rationale:* *CO was acceptable at baseline; all 6 tuning trials focused on pushing *H above +0.33 eV without shifting *CO out of window. +5%: $E(*H) = +0.252$ (low; strain to weaken H binding). -5%: $E(*H) = -0.066$ (low; opposite strain worsened). Sc→La doping +5%: $E(*H) = +0.316$ (low; more electropositive B-site nearly reached threshold). Additional trials with Sc→Y (+5%) and Sc→La (+6%) also fell short. **No success.**

Au₃Y (111). *Rationale:* compressive strain raised *H toward the threshold but simultaneously weakened *CO out of the target window, preventing a joint pass. +3%: CO too weak (-0.495 eV). +5%: CO too weak (-0.478 eV). Y→Sc +5%: CO too weak (-0.480 eV). **No success.**

In₃La (111). *Rationale:* *CO was in-range at baseline (-0.591 eV); tuning targeted weakening *H via strain and by swapping La→Y to change local electron donation. +5%: $E(*H) = +0.194$ (low; strain insufficient). La→Y +5%: $E(*H) = +0.155$ (low; different rare earth did not help). **No success.**

Al₃Rh (111). *Rationale:* near-miss (*H = +0.291 eV at base); tested gentle strain ($\pm 3\%$, +6%, +8.5%, -5%) and Rh→Ag substitution. More aggressive strain destabilized *CO without rescuing *H. +3%: $E(*H) = +0.303$ (low). Rh→Ag: $E(*H) = +0.277$ (low). +8.5%: $E(*CO) = -1.019$ (too strong). **No success.**

Al₃Ni (111). *Rationale:* inverse-failure case—*H already met the threshold (+0.351 eV at base) but *CO was too weak (-0.433 eV). Tuning targeted strengthening *CO without collapsing *H. Tensile strain pulled *CO in-range but *H fell below threshold; Ni→Fe overbound *CO; Ni→Rh with -1% strain was a near-miss. -3% tensile: $E(*CO) = -0.525$ (in-range) but $E(*H) = +0.278$ (low). Ni→Fe: $E(*CO) = -1.364$ (too strong). Ni→Rh -1%: $E(*CO) = -0.535$, $E(*H) = +0.311$ (low). **No success.**

Cd₃Pt (111). *Rationale:* both descriptors failed at base (*CO too strong, *H too favorable). Strain and Pt→Bi substitution at +3% brought *CO in-range (−0.751/−0.746 eV) but *H stayed strongly adsorbed (negative), indicating Pt-ensembles on Cd inherently bind H too strongly. +3%: $E(*\text{CO}) = -0.751$ (in-range), $E(*\text{H}) = -0.097$ (low). Pt→Bi +3%: $E(*\text{CO}) = -0.746$ (in-range), $E(*\text{H}) = -0.098$ (low). **No success.**

Cu (511). *Rationale:* canonical CO₂RR benchmark step surface; acceptable *CO (−0.638 eV) but *H far too favorable (−0.044 eV, HER-prone). Strain either worsened *CO or barely moved *H; Cu→Ag noble-metal dilution was insufficient. +5%: CO too strong (−1.016 eV). −5%: $E(*\text{H}) = -0.092$ (low). Cu→Ag: $E(*\text{H}) = +0.008$ (low). **No success.**

YN (110). *Rationale:* nitride baseline failed both descriptors (*CO = −0.401 eV too weak, *H = −0.241 eV too favorable). Y→Au substitution attempted to create a noble-metal-like surface site but did not shift either descriptor in the intended direction. Y→Au doping: $E(*\text{H}) = -1.260$ (worse). **No success.**

S4 Human-Ranked Materials from Agent Output

This section presents the final human-curated classification of Catalyst-Agent’s screening results into successful and unsuccessful candidates for each reaction. Successful candidates satisfy all target descriptor criteria (either in their pristine form or after agent-proposed surface modifications). The number of AdsorbML runs to first success is reported, where one “run” corresponds to a single tool call evaluating up to five Miller-index facets for a given material–modification combination.

S4.1 ORR: Successful and Failed Candidates

Table 11 lists the 28 materials that achieved at least one facet in the 0.9–1.1 eV Optimal window. Entries 1–18 are pristine (unmodified) successes; entries 19–28 required strain and/or surface substitution. Table 12 lists the materials that could not be tuned into the Optimal window despite multiple attempts, as well as Close/Near-band materials where the agent did not attempt iterative optimization. Note that CaTi_2O_6 (mp-1079825) is excluded from the failure table because it already achieved Optimal on its (210) facet (entry 9 in Table 11); only its Close-band (101) facet could not be further evaluated due to an AdsorbML error.

Table 11: Human-ranked ORR successes. Energies in eV.

#	Material	Identifier	Facet	E_{ads}	Modification	Runs
1	ZrO ₂	mp-2574	(200)	0.946	—	1
2	PbTiO ₃	mp-20459	(200)	0.987	—	1
3	SrTiO ₃	mp-5229	(001)	1.061	—	1
4	MgCo ₂ O ₄	mp-756442	(001)	0.920	—	1
5	SrNiO ₃	mp-762506	(210)	0.959	—	1
6	NiO	mp-1180047	(210)	0.948	—	1

Continued on next page

Table 11 continued

#	Material	Identifier	Facet	E_{ads}	Modification	Runs
7	CaNiO ₃	mp-1368210	(210)	0.996	—	1
8	ZnGa ₂ O ₄	mp-5794	(210)	1.042	—	1
9	CaTi ₂ O ₆	mp-1079825	(210)	0.976	—	1
10	RuO	oqmd-4372977	(210)	1.045	—	1
11	LaNiO ₂	mp-20392	(001)	0.946	—	1
12	BaFeO ₃	mp-19035	(111)	1.090	—	1
13	BaNiO ₃	mp-1120765	(111)	1.058	—	1
14	BaNiO ₂	mp-18943	(001)	1.046	—	1
15	SrMnO ₃	mp-19001	(001)	1.044	—	1
16	La ₂ NiO ₄	mp-21326	(001)	1.087	—	1
17	Pr ₂ NiO ₄	mp-18839	(001)	0.913	—	1
18	Gd ₂ NiO ₄	mp-1207225	(001)	1.075	—	1
<i>Tuned to Optimal via strain/doping</i>						
19	CaTiO ₃	mp-5827	(001)	0.991	−1% tensile	3
20	TiO ₂	mp-2657	(211)	1.048	−1% tensile	3
21	CoAl ₂ O ₄	mp-36447	(001)	1.095	+2% compressive	2
22	CoGa ₂ O ₄	mp-765466	(001)	1.058	−2% tensile	4
23	KNbO ₃	mp-7375	(111)	0.927	+3% compressive	2
24	Nd ₂ NiO ₄	mp-19191	(001)	1.088	Ni→Co, −1% tensile	6
25	SmNiO ₃	mp-1099668	(210)	0.907	−1.1% tensile	5
26	SmCoO ₃	mp-22549	(210)	1.068	Co→Fe doping	4
27	CaNi ₂ O ₅	mp-1410425	(111)	1.007	Ni→Co doping	2
28	PrCoO ₃	mp-20427	(111)	0.961	Co→Zn doping	4

Table 12: Human-ranked ORR failures—materials not reaching the 0.9–1.1 eV Optimal window (tuning-attempted and untreated Close/Near-band entries).

Material	Identifier	Summary
<i>Tuning attempted—failed</i>		
Co ₃ O ₄	mp-18748	Close (200) 0.889 eV; Co→Zn doping/−1% and −5% tensile could not raise energy above 0.9 eV. Prototypical Co-spinel with facet competition effects preventing success.
LaCuO ₃	mp-3474	Close (101) 1.108 eV; +1% compressive worsened to 1.461 eV. Cu-perovskite comparator where tuning destabilized key facets.
MnFe ₂ O ₄	mp-33708	Close (101) 0.877 eV; −3% tensile produced all weak or overbinding facets. Bimetallic Mn/Fe spinel where strain derailed adsorption across terminations.
CaNiO ₂	mp-1147749	Near (001) 1.237 eV; 3 doping trials (Ni→Co, Ni→Fe) did not reach Optimal. Reduced infinite-layer Ni phase where dopant knobs were insufficient.
Sr ₂ MnO ₄	mp-18978	Near (101) 0.746 eV; strain (+3%) and Mn→Ti doping insufficient. RP Mn oxide where layered structure precluded balanced binding.
SrRuO ₃	mp-22534	Near (001) 0.727 eV; −5% tensile reached only 0.877 eV. Ru-perovskite analogue that fell short of the target despite large strain.

FeO	mp-756436	Near (001) 0.778 eV; -5% tensile produced non-uniform response. Simple Fe ²⁺ oxide reference where strain effects were inconsistent across facets.
ZnAl ₂ O ₄	mp-2908	Near (001) 1.254 eV; $+5\%$ compressive worsened to 1.552 eV. Non-redox spinel where elastic tuning could not soften binding.

Close/Near band—not tuning-attempted

Sr ₂ NiO ₄	oqmd-5631134	Close (111) 0.833 eV. Alkaline-earth RP nickelate reference; no tuning attempted in this campaign.
NiFe ₂ O ₄	mp-22684	Near (001) 0.719, (200) 0.711 eV. Classic ferrite spinel; weak-binding.
LiFe ₂ O ₄	mp-25386	Near (001) 0.730 eV. Alkali-containing ferrite; weak-binding side.
CuFe ₂ O ₄	mp-770107	Near (001) 0.745 eV. Cu-containing ferrite; weak-binding side.
BiFeO ₃	mp-23501	Near (101) 0.791 eV. Polar/ferroelectric perovskite; moderately weak *OH.
MgO	mp-1265	Near (210) 1.243 eV. Simple ionic oxide reference; strong-binding side.
Ga ₂ O ₃	mp-1243	Near (111) 0.794 eV. Post-transition-metal oxide comparator.
TiFe ₂ O ₄	mp-780585	Near (001) 0.755 eV. Ti ⁴⁺ /Fe spinel; weak-binding side.
LaNiO ₃	mp-19339	Near (101) 1.284 eV. Flagship rare-earth nickelate; strong-binding.

SrCoO_3	mp-505766	Near (111) 0.703 eV. Co analogue of SrNiO_3 ; weak-binding side.
SrFeO_3	mp-510624	Near (001) 0.743 eV. Sr counterpart to BaFeO_3 ; moderately weak *OH.
Ba_2MnO_4	mp-753330	Near (101) 0.767 eV. Ba analogue of Sr_2MnO_4 ; weak-binding side.
NdNiO_3	mp-22106	Near (111) 0.700 eV. Nd analogue of LaNiO_3 ; weak-binding edge.
Gd_2CoO_4	oqmd-5233083	Near (111) 0.736 eV. Co-based RP analogue to Gd nickelates; weak-binding.

S4.2 NRR: Successful and Failed Candidates

Table 13 lists the 12 materials that satisfied both NRR descriptors ($E_N \in [-2.0, -0.5]$ eV and $\Delta > 0$ eV) on at least one facet, along with the number of AdsorbML runs (including the initial unmodified screening) required to reach the first success.

Table 13: Human-ranked NRR successes. Energies in eV.

#	Material	ID	Facet	E_N	E_{N_2}	Δ	Modification	Runs
1	CoNi	mp-1006883	(111)	-0.54	-0.65	+0.11	—	1
2	RhCo	mp-1226026	(100)	-0.63	-0.77	+0.14	—	1
3	IrMo	mp-1221414	(211)	-0.64	-0.76	+0.12	—	1
4	HfPd	mp-1002106	(211)	-1.84	-2.24	+0.40	—	1
5	PtFe	mp-2260	(111)	-0.79	-0.87	+0.08	+3% strain	2
6	FeNi	mp-2213	(100)	-0.92	-1.05	+0.13	—	1
7	Ni_4Mo	mp-11507	(111)	-0.61	-0.63	+0.02	Mo→Ni	4
8	IrRe	mp-1219533	(110)	-0.56	-0.70	+0.15	—	1
9	CoPt	mp-1225998	(100)	-0.64	-0.73	+0.10	Pt→Fe, +3%	5
10	PdRu	mp-1186459	(100)	-0.62	-0.84	+0.22	Pd→Fe	3

Table 13 continued

#	Material	ID	Facet	E_N	E_{N_2}	Δ	Modification	Runs
11	TiPt ₃	mp-12107	(110)	-0.50	-0.85	+0.35	Pt→Fe	3
12	PtRh	mp-1219734	(100)	-0.55	-0.60	+0.05	Pt→Fe	2

NRR failures. The following 40 materials could not achieve $\Delta > 0$ with E_N in-window on any tested facet despite strain and doping trials: Pd₃Mo, PdFe, CuFe (borderline; $\Delta > 0$ only at +12% strain), CoRu, Ni₂Mo, RuFe, RuPt, FeMo (overbinding on re-run), ZrPt (Δ too negative on re-run), Pt₃Co, CrPt, OsPt₃, HfPt, Ta₃Pt, MnPt, PdRe, PdNi, CuPd, Cu₃Pd₂, CuPd₃, ZrPd, CuZn, Cu₃Zn, CuZn₃, CuNi, CoCu, AuCu, CuMo, Fe₂Co, FeCo, FeW, WNi, RuAu, GaIr, AuPt, AuPd, MoW, MoV, VW, VCr.

S4.3 CO₂RR: Successful and Failed Candidates

Table 14 lists the 4 materials that passed both CO₂RR descriptors ($E_{\text{ads}}(*\text{CO}) \in [-0.82, -0.52]$ eV and $E_{\text{ads}}(*\text{H}) \geq +0.33$ eV). Formation energies from the Materials Project are included as an additional stability indicator. All successful structures share the $Pm\bar{3}m$ space group. Table 15 lists the materials that did not pass.

Table 14: Human-ranked CO₂RR successes. Energies in eV.

#	Material	Facet	$E(*\text{CO})$	$E(*\text{H})$	E_f [eV/at]	Modification
1	Pb ₃ Y	(111)	-0.738	+0.379	-0.287	—
2	Tl ₃ La	(111)	-0.619	+0.332	-0.347	+5% strain
3	Sn ₃ Y	(111)	-0.620	+0.513	-0.495	—
4	Sn ₃ Sc	(111)	-0.730	+0.465	-0.335	—

Table 15: Human-ranked CO₂RR failures.

#	Material	Facet	Summary
1	Au ₃ Sc	(111)	CO in-range but $E(*H)$ remained $< +0.33$ eV despite 6 strain/doping trials (best: Sc→La +5%, $E(*H) = +0.316$).
2	Cd ₃ Pt	(111)	Both descriptors failed at base; CO too strong (-0.894 eV). Strain/doping brought CO in-range but $E(*H)$ stayed negative.
3	Au ₃ Y	(111)	CO in-range but $E(*H) = -0.22$ eV. Compressive strain pushed CO out of range.
4	In ₃ La	(111)	CO in-range but $E(*H) = +0.12$ eV. Strain and La→Y doping insufficient.
5	In ₃ Y	(111)	PASS at +8.5% strain (listed in success table); base failed with $E(*H) = +0.17$.
6	Al ₃ Rh	(111)	Near-miss ($E(*H) = +0.291$); all trials fell short of +0.33.
7	Al ₃ Ni	(111)	Inverse failure: $E(*H)$ met threshold but CO too weak (-0.433 eV). Tensile strain brought CO in-range but $E(*H)$ collapsed.
8	Cu	(511)	CO in-range but $E(*H) = -0.044$ eV; strain/doping could not raise $E(*H)$ above +0.33.
9	YN	(110)	Both descriptors failed; doping (Y→Au) worsened $E(*H)$ to -1.26 eV.

S5 Predictive performance of UMA for catalysis: OC20 and AdsorbML benchmarks

The feasibility of closed-loop catalytic screening depends on the accuracy and the fidelity of the backbone machine-learning interatomic potential’s predictions of adsorption energetics and forces across varied adsorbate-surface systems. UMA models²⁵ provide a solid foundation for this purpose. These models achieve low total-energy and force errors on the OC20 dataset,⁷⁶ which is a large-scale adsorption dataset based on DFT relaxations. They also improve adsorption energy prediction quality relative to prior baselines. Table 16 reports OC20 validation errors for total energy (in-distribution and out-of-distribution splits) and OC20 test errors for adsorption energy, where adsorption energy is computed as a difference of two total-energy calculations (clean slab and adsorbate-slab). This is a formulation that empirically improves the accuracy of the adsorption-energy predictions over prior models.

Beyond pointwise energy and force MAE predictions, catalytic screening requires the determination of the global minimum energy across many adsorbate candidate placement sites. The AdsorbML enables the finding of this global minimum. A practical limitation of the original benchmark is the necessity of a downstream DFT evaluation of the ML-predicted global minima energy structure. To improve accessibility for those without the high-throughput DFT infrastructure, the ML-only variant replaces the DFT re-evaluation and is considered successful if the predicted energy is within 0.1 eV of the DFT minimum. This framework is well-aligned with Catalyst-Agent’s deployment setting, where the agent must repeatedly generate and relax many adsorbate-catalyst geometries and then proceed with further decisions based on the minimum-energy predictions. Taken together, the OC20 evaluation metrics and AdsorbML pipeline motivate UMA as an effective MLIP backbone model for autonomous catalyst screening.

Table 16: Catalysis validation and test results on OC20 metrics. All energies are in meV and forces are in meV/Å.

Model	<i>Val (Total Energy)</i>						<i>Test (Ads. Energy)</i>			
	ID			OOD-Both			ID		OOD-Both	
	Energy	Forces	Force Cosine	Energy	Forces	Force Cosine	Energy	Force	Energy	Force
UMA										
UMA-S	63.6	24.1	0.63	107.0	29.2	0.65	52.1	24.3	70.2	30.9
UMA-M	43.1	15.8	0.73	70.0	19.2	0.75	33.4	16.0	46.5	21.0
UMA-L	32.6	12.0	0.77	49.8	14.5	0.79	32.4	12.2	43.5	15.9
Literature										
eqV2-OC20 ²⁰	–	–	–	–	–	–	149.1	11.63	306.5	15.74
GemNet-OC20 ⁷⁷	–	–	–	–	–	–	163.5	16.33	343.3	23.11

S6 Token consumption and costs

Table 17: Token usage: Both inputs and outputs with costs

Date	Model	Input	Output	Cost (USD)
Dec 11, 2025	gpt-5.2	1,916,125	109,717	\$10.98
Dec 12, 2025	gpt-5.2	29,192	5,594	\$0.14
Dec 13, 2025	gpt-5.2	1,394,281	233,962	\$12.48
Dec 14, 2025	gpt-5.2	364,306	36,127	\$1.68
Dec 15, 2025	gpt-5.2	593,190	58,199	\$2.32
Dec 16, 2025	gpt-5.2	457,457	140,810	\$2.76
Dec 17, 2025	gpt-5.2	183,519	1,542	\$0.27
Dec 18, 2025	gpt-5.2	43,554	17,653	\$0.42
Dec 19, 2025	gpt-5.2	337,487	34,899	\$2.06
Dec 20, 2025	gpt-5.2	138,698	21,073	\$0.62
Dec 21, 2025	gpt-5.2	1,180,587	250,224	\$6.69
Dec 22, 2025	gpt-5.2	1,774,997	219,064	\$11.43
Dec 23, 2025	gpt-5.2	186,313	34,148	\$1.02
Dec 24, 2025	gpt-5.2	869,371	95,497	\$5.65
Dec 25, 2025	gpt-5.2	645,791	125,096	\$2.74
Jan 07, 2026	gpt-5.2	168,965	16,754	\$0.63
Jan 12, 2026	gpt-5.2	571,119	89,322	\$3.56
Jan 13, 2026	gpt-5.2	257,068	48,103	\$1.46
Feb 05, 2026	gpt-5.2	107,268	50,044	\$1.11
Total		11,219,288	1,587,828	\$68.00

TOC Graphic

